

# Accurate numerical approximation of the absolute stability of unbounded flows

Koen J. Groot<sup>a,\*</sup>, Henk M. Schuttelaars<sup>b</sup>

<sup>a</sup>AWEP Department, Section of Aerodynamics, Delft University of Technology, Kluyverweg 1, 2629HS Delft, The Netherlands

<sup>b</sup>Delft Institute of Applied Mathematics, Delft University of Technology, Van Mourik Broekman 6, 2628XE Delft, The Netherlands

## ARTICLE INFO

### Article history:

Received 1 February 2019

Received in revised form 5 August 2019

Accepted 6 October 2019

Available online 17 October 2019

Communicated by K. Promislow

### Keywords:

Streamwise BiGlobal stability problem

Advection-diffusion equation

Absolute spectrum

Numerical method

Symmetrization

## ABSTRACT

The initial stage of the laminar–turbulent transition of semi-infinite flows can be characterized as either an absolute or convective instability, naturally associated with localized wave packets. A convective instability is directly linked to an absolute instability in a different reference frame. Therefore, our aim is to determine the absolute stability of a flow in a given but arbitrary reference frame, which can only be directly inferred from the absolute eigenvalue spectrum. If advective processes are present, the associated absolute eigenfunctions grow exponentially in space in the advective direction. The eigenvalue spectrum is usually computed numerically, which requires truncating the domain and prescribing artificial boundary conditions at these truncation boundaries. For separated boundary conditions, the resulting spectrum approaches the absolute spectrum as the domain length tends to infinity. Since advective processes result in spatially exponentially growing eigenfunctions, it becomes increasingly difficult to represent these functions numerically as the domain length increases. Hence, a naive numerical implementation of the eigenvalue problem may result in a computed spectrum that strongly deviates from the (mathematically correct) absolute spectrum due to numerical errors. To overcome these numerical inaccuracies, we employ a weighted method ensuring the convergence to the absolute spectrum. From a physical point of view, this method removes the advection-induced spatial exponential growth from the eigenfunctions. The resulting (absolute) spectrum allows for a direct interpretation of the character of the pertinent perturbations and the eigensolutions can be used to construct and analyse the evolution of localized wave packets in an efficient way.

© 2019 The Authors. Published by Elsevier B.V. This is an open access article under the CC BY license (<http://creativecommons.org/licenses/by/4.0/>).

## 1. Introduction

Classifying the growth and the character of unstable perturbations on wall-bounded flows is the central goal of linear stability theory in aerospace applications. The stability methods typically used are based on eigenvalue problems including the classical Linear Stability Theory (LST, Mack [1]; Reed et al. [2]) for one-dimensional problems and BiGlobal stability analysis for two-dimensional flows, see Theofilis [3].

For flows on a semi-infinite domain, the stability is assessed via perturbations with a finite support; wave packets having a front in the up- and downstream direction. Using these perturbations, the stability of a flow can be characterized as absolute or convective, see Huerre and Monkewitz [4]; Schmid and Henningson [5]; Chomaz [6]. Absolute instability is determined by the amplitude evolution of a wave packet whose up- and downstream fronts propagate toward infinity in their respective direction. Note that this requires selecting a fixed reference

frame. Using this definition of absolute instability, it follows that, in the selected fixed reference frame, the flow is: (I) absolutely unstable, if at least one such wave packet grows in time; (II) absolutely stable, if all such wave packets decay in time; (III) convectively unstable, if the flow is absolutely stable in the fixed reference frame, but absolutely unstable in at least one other reference frame; (IV) absolutely and convectively stable, if there is no reference frame in which the flow is absolutely unstable. From this classification, it follows that assessing the possible absolute stability of a flow in an arbitrary reference frame is key.

The finite support of the wave packets is required in the above classification, because the propagation direction of fronts in the physical domain has to be assessed and this is impossible if the fronts are located at infinity. The LST and BiGlobal methods do not directly give the desired information, because the eigensolutions do not necessarily fulfil this requirement. In particular, the approaches yield, apart from possible discrete modes that *do* have localized eigenfunctions, a continuous spectrum as the domain length tends to infinity. The latter eigensolutions are referred to as continuum modes. The eigenfunctions corresponding to these

\* Corresponding author.

E-mail address: [k.j.groot@tudelft.nl](mailto:k.j.groot@tudelft.nl) (K.J. Groot).

modes have an infinite support. This spatially unconfined nature prohibits the physical interpretation of individual continuum modes as convective or absolute perturbations.

The bridge to extract the stability characteristics of wave packets from continuum modes is provided by applying Briggs's method, as described in the detailed treatments by Briggs [7]; Huerre and Monkewitz [8]; Brevdo [9]; Schmid and Henningson [5]. This method constructs spatially localized wave packets by superposing spatially unconfined continuum modes through the inverse Fourier transform integral. This translates naturally into interpreting a sum of modes, instead of each mode individually, as a physically relevant perturbation. Briggs's criterion for absolute instability relies on finding a branch point in the frequency spectrum, see §7.1.3 in Groot [10]. This point directly indicates the absolute stability of the flow. In particular, if the branch point lies in the (un)stable half of the complex frequency plane, the flow is absolutely (un)stable. Kapitula and Promislow [11, def. 3.2.5] indicate that branch points belong to the so-called absolute spectrum.

In general, no analytical expressions can be found for the spectrum, so numerical approaches have to be resorted to. This requires the truncation of the domain and the introduction of artificial boundary conditions. The spectrum of the resulting problem must converge as the domain length approaches infinity. Restricting ourselves to base flows that approach their asymptotic states in space at least exponentially, it is mathematically proven by Sandstede and Scheel [12, th. 5], that the spectrum converges to the absolute spectrum as the domain length tends to infinity when imposing separated truncation boundary conditions. Therefore, to determine the absolute stability of a flow, one has to impose separated truncation boundary conditions. Extracting the absolute stability information from the continuous spectrum this way was not yet properly understood before.

Previous numerical experiments indicate, however, that domain length convergence studies are very challenging [13–16]. It is even stated by Theofilis [3] that: 'the discretized approximation of the continuous spectrum will always be under-resolved.'

In view of the above, the aim of this paper is to accurately determine the absolute spectrum and corresponding eigenfunctions, given a reference frame. The absolute spectrum allows for a direct identification of the most unstable or least stable wave packet via its branch points and a direct classification of the flow as absolutely (un)stable.

A model problem representative for flow stability analyses is introduced in Section 2. The physical origin of the numerical issues is identified by assessing the model problem analytically in Section 3 and a solution method is proposed in Section 4. The problem with constant and varying coefficients is treated numerically in Section 5, allowing the investigation of the implications for numerical methods. The evolution of a wavepacket is elaborated on in Section 6. The paper is concluded in Section 7.

## 2. Model problem

In general, incompressible flow fields are governed by the Navier–Stokes equations. Here, the non-parallel self-similar flow over a flat-plate (Blasius flow) is considered, that satisfies the Navier–Stokes equations up to the boundary-layer approximations, see White [17, chapter 4] for a detailed elaboration. Let  $x$ ,  $y$  and  $z$  denote the streamwise, wall-normal and spanwise coordinates and  $\bar{U}$ ,  $\bar{V}$  and  $\bar{W}$  the  $x$ -,  $y$ - and  $z$ -components of the base flow velocity, respectively. The velocity components are assumed to be functions of  $y$  only. At the flat-plate,  $y = 0$ , the velocity components satisfy the no-slip boundary condition, i.e. they are zero. For the Blasius problem,  $\bar{W}(y) \equiv 0$  and  $\bar{U}(y)$  and  $\bar{V}(y)$  approach positive asymptotic (edge) values  $\bar{U}_e > 0$  and  $\bar{V}_e >$

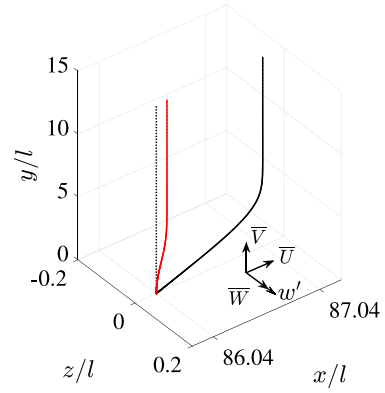


**Fig. 1.** Definition of the velocity variables and  $\bar{U}/\bar{U}_e$  (black) and  $10\bar{V}/\bar{U}_e$  (red),  $\bar{W} \equiv 0$ , boundary-layer velocity profiles, see Table 1.

0 as  $y \rightarrow \infty$ , see Fig. 1. The asymptotic values are approached super-exponentially, so that the requirements for the theorems of Sandstede and Scheel [12] are satisfied, see also Kapitula and Promislow [11, def. 3.1.1].

A base flow solution is not necessarily stable. To determine its stability, the base flow solution is perturbed. Perturbations are considered whose structure is constant in  $z$ . The infinitesimal perturbation to the spanwise velocity component, which is denoted by  $w'$ , is governed by the linearized Navier–Stokes  $z$ -momentum equation. Under the aforementioned assumptions, this equation reduces to:

$$\mathcal{L} \left( -i \frac{\partial}{\partial x}, -i \frac{\partial}{\partial y}, i \frac{\partial}{\partial t} \right) w' = \left( \frac{\partial}{\partial t} + \bar{U}(y) \frac{\partial}{\partial x} + \bar{V}(y) \frac{\partial}{\partial y} - \nu \left( \frac{\partial^2}{\partial x^2} + \frac{\partial^2}{\partial y^2} \right) \right) w' = 0. \quad (1)$$

Here,  $t$  is time and  $\nu$  is the kinematic viscosity.

The following Fourier ansatz can be imposed for the temporal and  $x$ -structure of  $w'$ :

$$w'(x, y, t) = e^{i\alpha x} \int_{-\infty+i\gamma}^{\infty+i\gamma} \tilde{w}(y; \omega) e^{-i\omega t} \frac{d\omega}{2\pi} + c.c., \quad (2)$$

where  $\tilde{w}$  is the perturbation amplitude,  $\alpha$  the streamwise wavenumber,  $\omega$  the (angular) frequency,  $\gamma$  the distance of the integration contour from the real  $\omega$ -axis and  $c.c.$  denotes the complex conjugate of the right hand side. The ansatz is discrete in  $\alpha$  and continuous in  $\omega$ , prescribing a non-localized structure in  $x$  and a localized structure (finite support) in  $t$ . A generic perturbation structure is allowed in  $y$ .

Substituting ansatz (2) into Eq. (1) yields

$$\tilde{\mathcal{L}} \left( -i \frac{d}{dy}; \alpha, \omega \right) \tilde{w} = \left( -i\omega + i\alpha \bar{U}(y) + \bar{V}(y) \frac{d}{dy} + \nu \left( \alpha^2 - \frac{d^2}{dy^2} \right) \right) \tilde{w} = 0, \quad (3)$$

a non-parallel version of the Squire equation, see Schmid and Henningson [5, p. 57].

At  $y = 0$ , a no-slip (homogeneous Dirichlet) condition is applied,  $\tilde{w}(0) = 0$ , consistent with the condition for the base flow. As deduced in the introduction, the perturbation solution must decay as  $y \rightarrow \infty$  in order to be interpreted as a physical perturbation and to be used to deduce the absolute or convective instability character of the flow in the  $y$ -direction. Every spatial direction can be treated separately in this regard. Note that the imposed non-localized nature of the solution in the  $x$ -direction precludes

deducing the absolute or convective instability character of the solution in that direction.

Analytical solutions usually cannot be found, hence numerical approximations are constructed. This requires the truncation of the domain at a finite length  $L$  and the introduction of an artificial boundary condition. It can be deduced from the mathematical literature, principally consisting of the work of Sandstede and Scheel [12], that two kinds of boundary conditions can be distinguished in general: separated and periodic boundary conditions. A separated boundary condition is a condition that does not link solution information at opposite boundaries, such as Dirichlet, Neumann or Robin type conditions; it specifies a relationship for the solution evaluated at one particular boundary. Obviously, periodic boundary conditions do link solution information at opposite boundaries and are an example of non-separated boundary conditions.

Sandstede and Scheel [12] prove that the use of *any type* of separated (Dirichlet, Neumann or Robin type) boundary condition yields a spectrum that dictates the absolute stability as  $L \rightarrow \infty$ . *The absolute stability of the system is of interest, therefore a homogeneous Neumann condition,  $d\tilde{w}/dy(L) = 0$ , is chosen, simulating (artificial) standing wave behaviour at  $y = L$ .* The theorems of Sandstede & Scheel will now be exemplified by assessing the constant-coefficient version of the model problem (3).

### 3. Algebraic spectrum analysis

As mentioned in the introduction, the current aim is to determine the absolute stability characteristics of a system based on its continuum solutions; i.e. the solutions that belong to the continuous spectrum. The Weyl essential spectrum theorem, see Kapitula and Promislow [11, theorem 2.2.6] and Kato [18, chapter 4, theorem 5.35], dictates that a system's continuum solutions depend only on the spatial asymptotic states of the system. That is, the continuum solutions depend on the boundary-layer edge values *only*, the precise shape of the velocity profiles near the wall is immaterial. So, it suffices to study the problem evaluated at the constant background velocity profiles,  $\bar{U} = \bar{U}_e$  and  $\bar{V} = \bar{V}_e$ . The resulting constant-coefficient problem can be solved analytically, by posing a Fourier ansatz in all independent variables for  $w'$ :

$$w'(x, y, t) = e^{i(\alpha x + ky - \omega t)} + c.c. \quad (4)$$

Note that for negative (positive)  $k_i$ ,  $w'$  grows (decays) in the positive  $y$ -direction. Therefore  $-k_i$  is from now on referred to as the growth rate (as opposed to a decay rate).

Substituting ansatz (4) into Eq. (1) yields

$$-i\omega + i\alpha\bar{U}_e + ik\bar{V}_e + v(\alpha^2 + k^2) = 0,$$

see Bouthier [19]. Grosch and Salwen [20] considered the equivalent with  $\bar{V}_e = 0$ . Solving  $\omega$  for given  $k$ , yields

$$\Omega(k) = \alpha\bar{U}_e + k\bar{V}_e - iv(\alpha^2 + k^2), \quad (5a)$$

and solving for  $k$ , given  $\omega$ , results in

$$\kappa_{1,2}(\omega) = -\frac{\bar{V}_e}{2v} \pm i \sqrt{\left(\frac{\bar{V}_e}{2v}\right)^2 + v^{-1}(-i\omega + i\alpha\bar{U}_e + v\alpha^2)}. \quad (5b)$$

For arbitrary  $k \in \mathbb{C}$ , it can be shown that

$$\kappa_{1,2}(\Omega(k)) = \begin{cases} +k \\ -k - i\bar{V}_e v^{-1} \end{cases}. \quad (6)$$

This clearly shows that, for a frequency  $\Omega(k)$  corresponding to a given  $k \in \mathbb{C}$ , another complex wavenumber, given by  $-k - i\bar{V}_e/v$ , exists that belongs to a perturbation with the same frequency  $\Omega(k)$ . This is demonstrated as follows:

$$\Omega(k) = \alpha\bar{U}_e + k\bar{V}_e - iv(\alpha^2 + k^2) \quad (7)$$

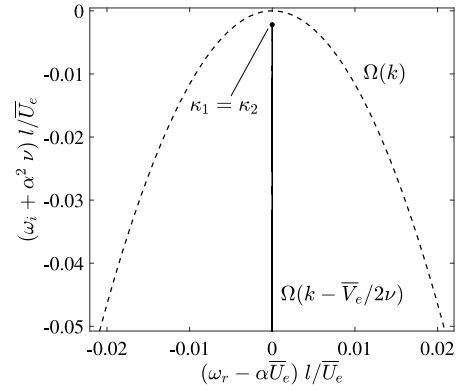


Fig. 2. Absolute (solid) and essential (dashed) spectrum limits ( $k \in \mathbb{R}$ ) corresponding to the parameters in Table 1. Branch point (•).

$$\begin{aligned} &= \alpha\bar{U}_e - k\bar{V}_e - i\bar{V}_e^2 v^{-1} - iv(\alpha^2 + k^2 + 2ik\bar{V}_e v^{-1} + i^2\bar{V}_e^2 v^{-2}) \\ &= \Omega(-k - i\bar{V}_e v^{-1}). \end{aligned}$$

An eigensolution, with a specific frequency  $\Omega(k)$ , is constructed by combining both homogeneous solutions corresponding to this frequency. The combination of the two solutions has to satisfy the boundary conditions. For  $k \in \mathbb{C}$ , this results in

$$\underbrace{(Ae^{iky} + Be^{i(-k - i\bar{V}_e/v)y})}_{\tilde{w}(y)} e^{i(\alpha x - \Omega(k)t)}, \quad (8)$$

where  $A$  and  $B$  are determined by the boundary conditions. As can be interpreted from Sandstede and Scheel [12], one only has to distinguish between separated and periodic boundary conditions, for each case yields a different limit of the spectrum as the domain length tends to infinity, namely the absolute and essential spectrum. These limits are detailed in what follows, specializing the description to the current model problem; a second order differential equation. The definitions and theorems directly generalize to differential equations with a higher order, see Sandstede and Scheel [12]; Kapitula and Promislow [11].

#### 3.1. Absolute spectrum limit

Sandstede and Scheel [12] prove (cf. theorem 5) that the spectrum approaches the so-called *absolute spectrum* limit as the domain length tends to infinity if the problem is equipped with separated (i.e. any choice of Dirichlet, Neumann or Robin) boundary conditions. This result is algebraically reproduced by Groot [10, §8.3.1] for the current model problem. Sandstede & Scheel define the absolute spectrum (see also Kapitula and Promislow [11, def. 3.2.3]) as the spectrum with  $\omega$ -values that satisfy

$$\kappa_{1,i}(\omega) = \kappa_{2,i}(\omega), \quad (9)$$

where  $\kappa_{1,2}$  are defined in Eq. (5b) and  $\kappa_{1,i}$  ( $\kappa_{2,i}$ ) refers to the imaginary part of  $\kappa_1$  ( $\kappa_2$ ). The corresponding eigenfunctions are here referred to as the *absolute eigenfunctions*. It follows from Eq. (6) that Eq. (9) holds when  $k_i = -\bar{V}_e/2v$ , for all  $k_r \in \mathbb{R}$ . In the  $\omega$ -plane, the absolute spectrum can accordingly be expressed as:

$$\begin{aligned} &\text{Absolute spectrum:} && \Omega(k_r - i\bar{V}_e/2v), \quad \text{for } k_r \in \mathbb{R}. \\ &(\text{separated conditions}) \end{aligned} \quad (10)$$

The locus of  $\Omega(k - i\bar{V}_e/2v)$  traced in the  $\omega$ -plane for  $k \in \mathbb{R}$  is shown as the solid line in Fig. 2 for the parameters given in Table 1. Shifts are applied to cancel the terms containing  $\alpha$ .

By substituting  $k_i = -\bar{V}_e/2\nu$  into Eq. (8), it follows that the *absolute eigenfunctions* of Eq. (3) display an *exponential spatial growth* for  $y \rightarrow \infty$ . An explanation for this spatial structure of the solutions is given in Appendix A. In Section 5, it will be illustrated that this inherent spatial growth renders numerically resolving these solutions very challenging, especially for large  $L$ , see Rodríguez et al. [15].

### 3.2. Essential spectrum limit

If periodic boundary conditions are applied, instead, Sandstede and Scheel [12] prove (cf. theorem 4) that the spectrum approaches a different limit as  $L \rightarrow \infty$ : the so-called *essential spectrum* (in an unweighted space). This result is also algebraically reproduced by Groot [10, §8.3.2] for the current model problem. The essential spectrum (see also Kapitula and Promislow [11, def. 2.2.3]) is defined by the spectrum with  $\omega$ -values for which

$$\kappa_{1,i}(\omega) = 0 \quad \text{or} \quad \kappa_{2,i}(\omega) = 0. \quad (11)$$

It follows from Eq. (6) that condition (11) is satisfied if  $k_i = 0$  or  $k_i = -\bar{V}_e/\nu$ , again for all  $k_r \in \mathbb{R}$ . Using Eq. (7), it follows that both cases result in the same locus in the  $\omega$ -plane:

$$\begin{array}{ll} \text{Essential spectrum:} & \Omega(k_r), \quad \text{for } k_r \in \mathbb{R}. \\ \text{(periodic conditions)} & \end{array} \quad (12)$$

This spectrum is shown as the dashed line in Fig. 2. It is important to observe that the essential spectrum attains larger  $\omega_i$ -values than those obtained in the absolute spectrum. A general property of the absolute spectrum is its minimal extent (e.g. upwards protrusion) in the  $\omega$ -plane, see Kapitula and Promislow [11, lemma 3.2.4]. For example,  $\max_{k_r} \Omega_i(k_r + i\phi)$  is minimal with  $\phi = -\bar{V}_e/2\nu$ . This minimal extent is the property that justifies the name ‘absolute’ [10, §7.4.2].

By substituting the values  $k_i = 0$  or  $k_i = -\bar{V}_e/\nu$  into Eq. (8), it follows that the *spatial exponential growth rate of the eigenfunctions associated to the essential spectrum is equal to zero*.

### 3.3. Branch points

Kapitula and Promislow [11, def. 3.2.5] define *branch points* as the  $\omega$ -values for which

$$\kappa_1(\omega) = \kappa_2(\omega). \quad (13)$$

As mentioned in the introduction, a branch point in the  $\omega$ -plane allows determining the absolute stability of a flow via Briggs’s criteria, see §7.1.3 in Groot [10]. For the current constant-coefficient model problem, the  $\omega$ -value satisfying condition (13), denoted by  $\omega_0$ , equals:

$$\omega_0 = \alpha \bar{U}_e - i\nu \left( \alpha^2 + \left( \frac{\bar{V}_e}{2\nu} \right)^2 \right). \quad (14)$$

For non-zero  $\alpha, \bar{U}_e, \bar{V}_e \in \mathbb{R}$  and  $\nu > 0$ , it follows that  $\omega_{0,i} < 0$ , therefore the constant-coefficient model problem is absolutely stable under those conditions. This branch point is also indicated in Fig. 2.

Branch points are contained in the absolute spectrum, because Eq. (13) augments Eq. (9) by additionally requiring the equality of the real parts of  $\kappa_1$  and  $\kappa_2$ . As discussed in Section 3.1, Sandstede and Scheel [12] prove that applying separated boundary conditions results in the absolute spectrum. Therefore separated boundary conditions are to be used if the absolute stability characteristics are to be investigated.

For the current model problem with  $\bar{V}_e \neq 0$ ,  $\kappa_1(\Omega(k)) \neq \kappa_2(\Omega(k))$  for all  $k \in \mathbb{R}$ . Hence, the essential spectrum does not

contain branch points and Briggs’s criterion cannot be applied. It therefore *does not yield direct information* on the absolute stability of the flow. Nevertheless, from the knowledge that the absolute spectrum has a minimal extent, it follows that the essential spectrum cannot reach lower maximal  $\omega_i$ -values than the absolute spectrum. If the essential spectrum is found to be completely stable, therefore, the flow is absolutely stable. If the essential spectrum protrudes into the unstable half of the frequency plane, however, no conclusion can be drawn about the absolute stability of the flow, see figure 7.6 of Groot [10].

It is concluded that, to assess the absolute stability of a flow unequivocally, one must resolve the absolute spectrum, which requires applying separated boundary conditions.

## 4. Solution method: weighted formulation (symmetrization)

In approaching the problem numerically, one must resolve the absolute eigenfunctions, which grow exponentially in space. To circumvent the numerical problems associated with unbounded spatial growth, the  $\tilde{w}$  eigenfunctions are multiplied with an exponential weighting function  $\sigma = \sigma(y)$ . For general  $\bar{V} = \bar{V}(y)$ , this weighting function reads

$$\sigma = e^{-\int_0^y \bar{V}(\tilde{y}) d\tilde{y}/2\nu}. \quad (15)$$

The governing differential equation is retrieved by substituting  $\hat{w} = \sigma \tilde{w}$  into Eq. (3), forming what is referred to as the *conjugated operator*:  $\sigma \tilde{\mathcal{L}}(\sigma^{-1} \sigma \tilde{w}) = \sigma \tilde{\mathcal{L}}(\sigma^{-1} \hat{w}) \equiv \hat{\mathcal{L}}(\hat{w})$  (Kapitula and Promislow [11, pp. 53–54]; Sandstede and Scheel [12]):

$$\begin{aligned} \sigma \tilde{\mathcal{L}}(\sigma^{-1} \hat{w}) &= \sigma (-i\omega + i\alpha \bar{U}(y) + \nu\alpha^2) \sigma^{-1} \hat{w} \\ &\quad + \sigma \bar{V}(y) \frac{d\sigma^{-1} \hat{w}}{dy} - \sigma \nu \frac{d^2 \sigma^{-1} \hat{w}}{dy^2} = 0 \\ \hat{\mathcal{L}}(\hat{w}) &= \left( -i\omega + i\alpha \bar{U}(y) + \frac{\bar{V}^2(y)}{4\nu} - \frac{1}{2} \frac{d\bar{V}}{dy}(y) \right. \\ &\quad \left. + \nu \left( \alpha^2 - \frac{d^2}{dy^2} \right) \right) \hat{w} = 0. \end{aligned} \quad (16)$$

The Neumann boundary condition transforms to

$$\sigma \frac{d\sigma^{-1} \hat{w}}{dy} \Big|_{y=L} = \left( \frac{d\hat{w}}{dy} + \frac{\bar{V}(y)}{2\nu} \hat{w} \right) \Big|_{y=L} = 0. \quad (17)$$

The eigenvalue problem for  $\hat{w}$  (Eq. (16)) and  $\tilde{w}$  (Eq. (3)) with the associated boundary conditions is referred to as the *weighted* and *unweighted* problem, respectively.

Effectively, the advection term  $\bar{V}d/dy$  in Eq. (3) is replaced by the reaction term  $(\bar{V}^2/2\nu - d\bar{V}/dy)/2$  in Eq. (16). Removing the former term is, in fact, the recipe to deriving the expression for  $\sigma$ . The absolute (and discrete) spectrum of the operators  $\hat{\mathcal{L}}$  and  $\tilde{\mathcal{L}}$  is identical, see Kapitula and Promislow [11, lemma 3.2.4], and the eigensolutions are related as  $\hat{w} = \sigma \tilde{w}$ .

The weighted problem is a regular, self-adjoint Sturm–Liouville eigenvalue problem, see Haberman [21]. The eigenfunctions thus form an orthonormal basis:  $\langle \hat{w}_i, \hat{w}_j \rangle = \delta_{ij}$ , where  $\langle \cdot, \cdot \rangle$  is the  $L^2$ -function inner product and  $\delta_{ij}$  is the Kronecker delta. This approach is equivalent to the ‘symmetrization method’ treated by Reddy and Trefethen [22]. As noted in the same reference, the weighting function  $\sigma^{-1}$ , signifying eigenfunction growth in space, is the sole property that renders the eigenfunctions corresponding to the unweighted problem,  $\tilde{w}$ , to be mutually non-orthogonal. The direct relationship of the weighting function to the non-parallel advection  $\bar{V}$  in Eq. (15) illustrates how the non-orthogonality of the eigenfunction basis is, in turn, directly related to advection. A further physical interpretation of the weighted approach is given in Appendix A.



To illustrate that the spatial growth is cancelled from the asymptotic behaviour of the eigensolutions, Eq. (16) can again be considered with constant coefficients. Ansatz (4) is adapted to yield the weighted problem by incorporating the factor  $\sigma$  as follows:

$$w'(x, y, t) = \sigma^{-1}(y) e^{i(\alpha x + ky - \omega t)} + c.c. \quad (18)$$

Substitution into Eq. (1) yields:

$$\hat{\Omega}(k) = \alpha \bar{U}_e - i \frac{\bar{V}_e^2}{4\nu} - i\nu(\alpha^2 + k^2), \quad (19a)$$

$$\hat{k}_{1,2}(\omega) = \pm i \sqrt{\left(\frac{\bar{V}_e}{2\nu}\right)^2 + \nu^{-1}(-i\omega + i\alpha \bar{U}_e + \nu\alpha^2)}. \quad (19b)$$

A substitution reveals that  $\hat{k}_{1,2}(\hat{\Omega}(k)) = \pm k$ . Hence, by having included the factor  $\sigma$  in the ansatz,  $\hat{k}_1$  and  $\hat{k}_2$  have the same imaginary part only for  $k_i = 0$ . Condition (9) therefore implies that the absolute spectrum corresponds to  $k \in \mathbb{R}$  and that the spatial exponential growth rate of the  $\hat{w}$ -eigenfunctions is equal to zero.

To find the spectrum in the  $\omega$ -plane, one has to evaluate  $\hat{\Omega}(k)$  for  $k \in \mathbb{R}$ . By evaluating  $\Omega(k - i\bar{V}_e/2\nu)$ , it follows that:

$$\hat{\Omega}(k) = \Omega\left(k - i \frac{\bar{V}_e}{2\nu}\right), \quad (20)$$

i.e. the loci traced by  $\Omega(k - i\bar{V}_e/2\nu)$  and  $\hat{\Omega}(k)$  (for all  $k \in \mathbb{C}$ ) are the same. This is a demonstration of the more general fact (lemma 3.2.4 of Kapitula and Promislow [11]) that the absolute spectra in the  $\omega$ -plane corresponding to the weighted and unweighted problems are identical.

In conclusion, both the unweighted and weighted problems result in the same spectrum. However, numerical errors are expected to have a dominant impact when solving the unweighted problem for too large domain lengths. By annihilating the spatial exponential growth with the factor  $\sigma$ , i.e. using a weighted approach, that complication is entirely removed, resulting in accurate spectra and eigenfunctions. This will be demonstrated in the next section.

## 5. Computational spectrum analysis for large $L$

The main goal of this section is to test the performance of the method presented in Section 4 via numerical experiments. This pertains to the second objective mentioned in the introduction: to establish an adequate approach to numerically approximate the absolute spectrum encoding the absolute stability characteristics as  $L \rightarrow \infty$ .

As background flow profiles, the constant-coefficient case (Section 5.1) and non-parallel Blasius boundary-layer profile (Section 5.2) are considered. The eigenvalue problems are discretized using Chebyshev spectral collocation in  $y$ , using the standard cosine node distribution (see Canuto et al. [23]; Weideman and Reddy [24]). There is no reason to increase the node resolution at one boundary over that at the other in order to accurately represent the continuum solutions. Therefore, the use of grid mappings, such as the mapping introduced by Malik [25], is avoided. The boundary-layer profiles are interpolated onto these nodes using spline interpolation. The number of collocation nodes used in the interior of the domain is denoted by  $N$ . The discretized eigenvalue problem is solved using the QZ algorithm (see Golub and Van Loan [26]). Computed eigenvalues obtained from the discretized versions of equations ((3), i.e. the unweighted problem) and ((16), weighted) are denoted by  $\tilde{\omega}$  and  $\hat{\omega}$ , respectively.

**Table 1**

Reference simulation parameters.

$\bar{U}_e$ (m/s)	$l$ (m)	$\nu$ (m <sup>2</sup> /s)	$x/l = \bar{U}_e l/\nu$	$\bar{V}_e/\bar{U}_e$	$\alpha l$
15	$8.3792 \times 10^{-5}$	$1.4608 \times 10^{-5}$	86.040	0.01	$2\pi$

The domain length is denoted by  $L$ . The length scale used to make lengths non-dimensional is the local Blasius length scale and it is denoted by  $l$ . Seven domain lengths are considered:  $L/l = 60, 72, 90, \dots, 360$ , according to the rule  $360/5, 360/4, 360/3, \dots, 360/1$ , and  $L/l = 3600 = 360/0.1$ . This choice follows from the observation (shown later) that the spectra converge as  $1/L$ . If not indicated otherwise, the resolution is varied proportionally with  $L$ :  $N = L/l$ .

### 5.1. Constant-coefficient problem

First, the problem with the coefficients  $\bar{U}(y) = \bar{U}_e$  and  $\bar{V}(y) = \bar{V}_e$  is solved. The numerical results obtained for this constant-coefficient case can be directly compared with the analytical results presented in Section 3. The parameters  $\bar{U}_e$  and  $\bar{V}_e$  are obtained from the edge conditions corresponding to the Blasius boundary-layer indicated in Table 1. The parameter  $x/l$  is the non-dimensional downstream distance from the leading edge and  $\alpha l$  the non-dimensional streamwise wavenumber. The particular profile is chosen for which  $\bar{V}_e l/\nu = 1.7208/2$ .

#### 5.1.1. Weighted approach

The  $\hat{w}$ -eigenvalues computed using the weighted problem formulation for  $\hat{w}$  are shown as black symbols in Fig. 3 (a), i.e. the discretized version of Eq. (16) is solved for the different domain lengths. At the shown scale, the computed spectra are all indistinguishable from the exact absolute spectrum (the solid red line), given by  $\Omega(k - i\bar{V}_e/2\nu)$  evaluated for real  $k$ , see Eq. (5a). This includes the largest domain case, with  $L/l = N = 3600$ . The largest departures of the computed eigenvalues from the exact result are of  $O(10^{-13}l/\bar{U}_e)$  in absolute value, so the absolute spectrum is approximated virtually exactly.

Next to the eigenvalue spectra, the eigenfunctions are considered. The red lines in Fig. 4 are the functions  $\sigma^{-1}\hat{w}$ . Note that, while  $\hat{w}$  itself satisfies Eq. (16), the product  $\sigma^{-1}\hat{w}$  is an eigenfunction of Eq. (3) and therefore can be compared against the  $\tilde{w}$ -eigenfunctions later. When graphing the eigenfunctions, the maximum of their absolute values will always be scaled to unity. The functions are shown on a logarithmic scale in Fig. 4, this has the advantage that the slope of the graphs directly represents the spatial exponential growth rate of the functions. Amongst all available solutions, the zeroth harmonic is displayed, because it is most representative of the amplitude distribution of the other eigenfunctions. While having a very similar graph to the zeroth harmonic, the magnitudes of other harmonics oscillate and they therefore would unnecessarily complicate the figure. The eigenfunction  $\hat{w}$  is multiplied with the spatial growth function  $\sigma^{-1}$ ; no addition is required so that no underflow errors can occur. Hence, values smaller than  $10^{-15}$  can be represented numerically. Clearly, the considered domain lengths are so large that the magnitude of  $\sigma^{-1}\hat{w}$  near  $y = 0$  is smaller than machine precision. Due to the inherent spatial exponential growth imposed by  $\sigma^{-1}$ , the domain can always be made large enough that the function  $\sigma^{-1}\hat{w}$  attains much smaller magnitudes than the machine precision used. This preludes to the inherent difficulty faced when computing the  $\tilde{w}$ -eigenfunctions directly, by discretizing Eq. (3).

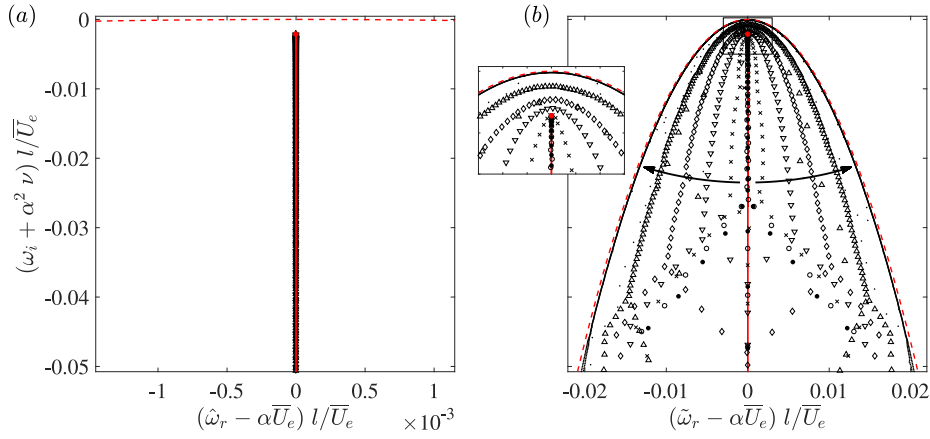


**Fig. 3.** Computed (a)  $\tilde{\omega}$ - and (b)  $\tilde{\omega}$ -spectrum for  $\bar{U} = \bar{U}_e$ ,  $\bar{V} = \bar{V}_e$  (symbols), branch point (red dot).  $L/l = 60$  (●), 72 (○), 90 (×), 120 (▽), 180 (◇), 360 (△), 3600 (·),  $N = L/l$ ,  $\bar{V}_e l/\nu = 1.7208/2$ . Algebraic essential spectrum (red dashed) and absolute spectrum (red solid). Arrows indicate the direction of increasing  $L$ . Inset in (b) shows a zoom on the box.

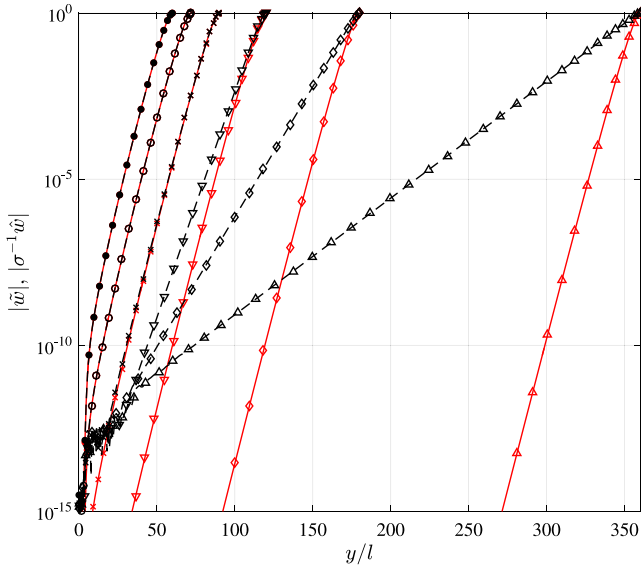


**Fig. 4.** Computed zeroth harmonic continuum modes  $|\tilde{w}|$  (dashed black, unweighted approach),  $|\sigma^{-1}\tilde{w}|$  (solid red, weighted approach) relative to their maximum absolute value, with  $L/l = N = 60$  (●), 72 (○), 90 (×), 120 (▽), 180 (◇) and 360 (△),  $\bar{V}_e l/\nu = 1.7208/2$ .

### 5.1.2. Unweighted approach

The  $\tilde{\omega}$ -eigenvalues computed using the unweighted approach for  $\tilde{w}$  are shown in Fig. 3 (b), i.e. the same domain lengths were considered, but now solving the discretized version of Eq. (3). Note that the  $\omega_r$ -axis is zoomed out with respect to that in Fig. 3 (a). For  $L/l = 60$  (●) and 72 (○), the  $\tilde{\omega}$ -spectrum lies close to the absolute spectrum. The pattern of these eigenvalue spectra corresponds closely to that found by Reddy and Trefethen [22], see their figure 6. For  $L/l \geq 90$  (×), the  $\tilde{\omega}$ -spectrum starts to deviate from the absolute spectrum, forming a parabolic shape. As shown in the inset, which provides a zoom onto  $\omega$ -plane indicated with the black box directly around the branch point, the uppermost eigenvalues have moved significantly up and away from the branch point for  $L/l = 120$  (▽). As  $L/l = N \rightarrow \infty$ , the spectrum approaches the curve  $\Omega(k)$  evaluated for real  $k$ ; the essential spectrum.

The finding that the computed  $\tilde{\omega}$ -spectrum does not approximate the absolute spectrum for too large  $L$  is an important one. It demonstrates that the computed spectrum can no longer be

used to deduce absolute stability information for the analysed problem.

To shed light on the behaviour of the  $\tilde{\omega}$ -spectra for  $L/l > 72$ , it is important to consider the eigenfunctions. The functions  $\tilde{w}$  are shown as the dashed black lines in Fig. 4. The computed unweighted  $\tilde{w}$ -eigenfunctions grow exponentially in space for large  $y/l$ . For  $L/l > 72$ , however, their spatial growth rate is increasingly less than the exact value  $-k_i = \bar{V}_e/2\nu$  corresponding to the absolute eigenfunctions. This is especially apparent when comparing the  $\tilde{w}$ -eigenfunctions against the products  $\sigma^{-1}\tilde{w}$  in Fig. 4, that are representative of the exact solution. The adapted growth rate is likely caused by the fact that the eigensolver cannot accurately represent  $|\tilde{w}|$ -values smaller than  $10^{-12}$ . In particular, it is observed that the functions  $\tilde{w}$  form approximately linear lines between the points  $(y, \log_{10} |\tilde{w}(y)|) \approx (30l, -12)$  and  $(L, 0)$ . Assuming that it holds for all large enough  $L$ , this observation implies that the spatial exponential growth rate of the  $\tilde{w}$ -eigenfunctions decays as  $1/L$  while increasing  $L$ . Note that the observation is independent of the used sequence of domain lengths for which the eigenvalue spectra were computed.

The spatial exponential growth rate of  $\tilde{w}$ -eigenfunctions is intimately linked with the  $\tilde{\omega}$ -spectrum. While the spatial growth rate deviates from the exact value  $\bar{V}_e/2\nu$  corresponding to the absolute eigenfunctions for large enough  $L$ , it matches with  $-\kappa_{1,i}(\tilde{\omega})$ . This was numerically verified by evaluating  $\kappa_{1,i}$ , see Eq. (5b), for the computed  $\tilde{\omega}$ -eigenvalues and comparing it against a measurement of the growth rate of the computed  $\tilde{w}$ -eigenfunction for large  $y/l$ . This implies that the computed eigensolutions still satisfy the dispersion relation (5a). Conversely, the  $\tilde{\omega}$ -spectrum could therefore be determined by evaluating  $\Omega$ , see Eq. (5a), for the complex wavenumber  $k$  corresponding to the computed  $\tilde{w}$ -eigenfunction.

The apparent satisfaction of the dispersion relation (5a) allows explaining the observed departure of the computed  $\tilde{\omega}$ -spectrum from the absolute spectrum and its convergence to the essential spectrum. For too large domain lengths, the growth rate of the  $\tilde{w}$ -solutions departs from the exact value  $-k_i = \bar{V}_e/2\nu$  and approaches zero as  $1/L$ . As known from the behaviour of the function  $\Omega(k)$ , the growth rate  $-k_i = \bar{V}_e/2\nu$  corresponds to the absolute spectrum (see Section 3.1), while a neutral growth rate corresponds to the essential spectrum (see Section 3.2). It follows therefore logically that, as  $L \rightarrow \infty$ , the  $\tilde{\omega}$ -spectrum departs from the absolute spectrum and approaches the essential spectrum as observed in Fig. 3 (b).

Extrapolating the current findings to more complicated flow stability analyses, the fact that the computed solutions do still

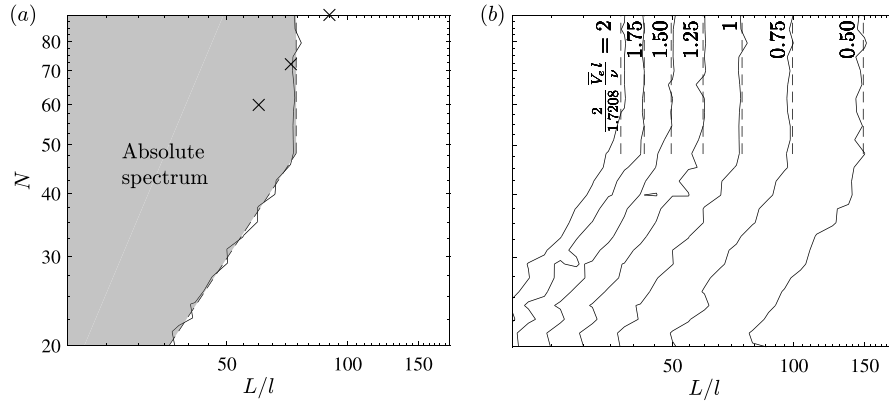


**Fig. 5.** Divergence boundary where the  $\tilde{\omega}$ -spectrum diverges from the absolute spectrum, if crossed towards the right. (a) Fixed  $\bar{V}_e l/v = 1.7208/2$ , cases  $L/l = N = 60, 72$  and  $90$  ( $\times$ ). (b) Varying  $\bar{V}_e l/v$ . Numerical results (solid lines) and fits with Eq. (22) and  $c(L/l)^{1.20}$  (dashed lines).

respect the dispersion relation explains the consistency of LST and PSE with BiGlobal stability results, as shown by Alizard and Robinet [14] and Rodríguez [27]. The computed BiGlobal spectra move upwards with  $L$ . This suggests that they have departed from the absolute spectrum, because the latter covers a minimal extent of the  $\omega$ -plane [11, lemma 3.2.4]. Although the spectra therefore do not represent the absolute stability characteristics, the satisfaction of the dispersion relation allows for their use in an eigenfunction expansion. It will be demonstrated in Section 6 that the use of the  $\tilde{\omega}$ -eigensolutions as an expansions basis can perform very poorly with respect to the  $\hat{\omega}$ -eigensolutions for the current model problem.

Reddy and Trefethen [22] link the exponential spatial growth of the eigenfunctions to resolvent estimates (cf. theorem 7). In turn, these estimates indicate the pseudospectrum levels, see Trefethen and Embree [28] for a definition, in the direct neighbourhood of  $\Omega(k_r - i\bar{V}_e/2\nu)$  decay exponentially with  $L$ . The presently computed pseudospectrum level below the branch point of the discretized operators is quite severe:  $O(10^{-16})$  for  $L/l > 72$ ; the pseudospectrum pushes the spectrum away from the absolute spectrum limit. Brynjell-Rahkola et al. [16] and Lesshaft [29] report similar levels below their computed spectra.

### 5.1.3. Domain length threshold for the unweighted approach

To isolate under what conditions the  $\tilde{\omega}$ -spectrum diverges from the absolute spectrum when computed numerically, simulations are performed while varying  $N$  and  $L$  independently. The locus of the points  $(L/l, N)$  is determined where  $\kappa_{1,i}(\tilde{\omega})$  deviates more than one percent from  $-\bar{V}_e/2\nu$ . This reliably indicates the deviation. The boundary in the  $(L/l, N)$ -space, to the left of which the absolute spectrum is adequately resolved, is indicated by the solid and dashed lines for the parameters in Table 1 in Fig. 5 (a). A clear twofold trend is observed, the first is linear on the double logarithmic scale and the other constant in  $L$ . The values of  $N$  and  $L/l$  used in Fig. 3 are indicated with the crosses. The cases  $L/l = 60$  and  $72$  lie to the left of the boundary. The case  $L/l = 90$  lies to the right, indicating the spectrum has departed significantly from the absolute spectrum.

This numerical evidence strongly suggests that, independently of  $N$ , the spectrum departs from the absolute spectrum if the problem is solved with the unweighted approach and with a domain length  $L$  larger than a certain threshold. In Fig. 5 (a), this threshold domain length, from now on denoted by  $L_{th}$ , is approximately  $74l$ . For  $N$  smaller than 48, the spatial resolution Nyquist limit controls the departure, resulting in a linear trend on the double logarithmic scale, relating  $N \sim (L/l)^{1.20}$ . The latter trend is expected to be dependent on the numerical discretization scheme deployed, while the  $L = L_{th}$  limit is expected to be

independent of the discretization method. Fig. 5 (b) indicates that both trends persist for other  $\bar{V}_e$ -values, while keeping all other parameters fixed. Specifically, the boundary moves to the left and right for larger and smaller values of  $\bar{V}_e$ , indicating self-similarity with the parameter  $\bar{V}_e L/v$ .

While varying  $\bar{V}_e$ , the relative magnitude of the eigenfunctions for the corresponding  $L_{th}$  values consistently yields:

$$e^{(\bar{V}_e l/2\nu) \times (L_{th}/l)} = O(10^{14}), \quad (21)$$

which is comparable to the reciprocal of the precision of the eigensolver  $\epsilon \|A\|_F$ , where  $\epsilon$  is the machine precision and  $\|A\|_F$  the Frobenius norm of the discretized operator matrix, see Anderson et al. [30]. Using this observation, an upper bound on the domain length,  $L_{th}$ , is synthesized:

$$\frac{L_{th}}{l} = -\ln(\epsilon \|A\|_F) \frac{\bar{V}_e l}{2\nu}. \quad (22)$$

By fitting the vertical dashed curve for the case  $\bar{V}_e l/v = 1.7208/2$  in Fig. 5 (a), the other dashed curves in Fig. 5 (b) follow from Eq. (22).

To summarize, for  $L < L_{th}$ , the absolute spectrum is retrieved by solving the discretized version of both Eqs. (3) and (16). For  $L > L_{th}$ , the spectrum computed with the unweighted approach deviates from the absolute spectrum and approaches the essential spectrum as  $L \rightarrow \infty$ . According to theorem 5 of Sandstede and Scheel [12], the computed spectrum should not approach the essential spectrum limit. This indicates that the numerical approximation fails when using the unweighted approach. The numerically infinitesimal magnitude of the eigenfunctions for small  $y/l$  indicates that this is a consequence of the combination of finite precision arithmetic and the spatial exponential growth inherent to the absolute eigenfunctions. By factoring the spatial growth, the weighted problem formulation avoids this numerical issue entirely. Accordingly, the spectrum computed with the weighted approach is found to overlap the exact absolute spectrum to eigensolver precision for all  $L$ .

These results convincingly demonstrate that the numerical issues encountered when computing the eigenvalue spectrum for large  $L$  are caused by the advection-induced spatial growth of the eigenfunctions. The weighted approach resolves this issue directly and therefore forms the method sought to fulfil the primary aim of this paper: to accurately determine the absolute spectrum and the corresponding eigenfunctions.

### 5.2. Varying-coefficient problem: Blasius boundary layer

An analytical solution was available for the constant-coefficient problem. As mentioned in the introduction, this case is

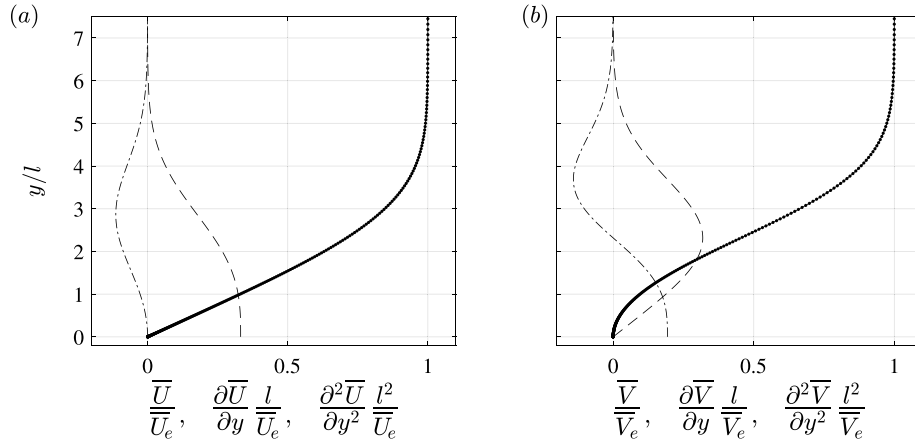


**Fig. 6.** Function (dotted, dots indicate nodes), first (dashed) and second (dash-dotted)  $y$ -derivative of (a)  $\bar{U}(y)$  and (b)  $\bar{V}(y)$ , see Table 1 for parameter values.

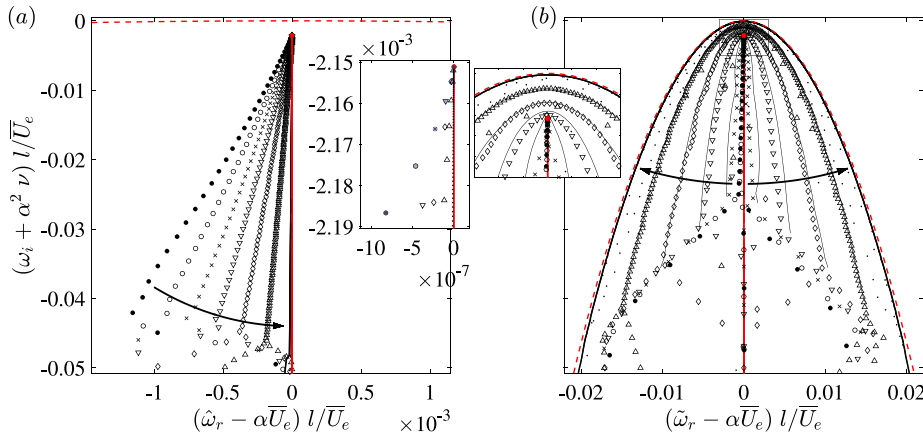


**Fig. 7.** Computed (a)  $\hat{\omega}$ - and (b)  $\hat{\omega}$ -spectrum for  $\bar{U} = \bar{U}(y)$ ,  $\bar{V} = \bar{V}(y)$  (symbols), branch point (red dot).  $L/l = 60$  ( $\bullet$ ),  $72$  ( $\circ$ ),  $90$  ( $\times$ ),  $120$  ( $\nabla$ ),  $180$  ( $\diamond$ ),  $360$  ( $\Delta$ ),  $3600$  ( $\cdot$ ),  $N = L/l$ ,  $\bar{V}_e l/\nu = 1.7208/2$ . Algebraic essential spectrum (red dashed) and absolute spectrum (red solid). Parabolic spectra excerpts for constant  $\bar{U}$ ,  $\bar{V}$  (solid black lines) from Fig. 3 (b). Arrows indicate the direction of increasing  $L$ . In (a), the inset shows a zoom on the values closest to the branch point, the last points belonging to a particular computed spectrum are coloured blue. In (b), the inset shows a zoom on the box.

quite unusual. To demonstrate the applicability of the findings for the constant-coefficient problem in a more complicated setting, a varying-coefficient case is considered for which no analytical solution is available.

The Blasius boundary layer provides a realistic set of inhomogeneous  $\bar{U}$  and  $\bar{V}$  profiles. The steady boundary-layer equations were solved using second-order finite differences in  $x$  and Chebyshev spectral collocation in  $y$ . To be abundantly sure of having a machine precision accurate solution, 400 nodes are used in the wall-normal direction, deploying a mapping to densely resolve the neighbourhood of the boundary. The equations are solved by marching in the  $x$ -direction, starting with the Blasius self-similar solution at  $x/l \approx 1$  up to  $x/l = \bar{U}_e l/\nu$  as given in Table 1, yielding exactly the same parameters as for the constant-coefficient problem. The resulting profiles are shown in Fig. 6. The boundary-layer thickness,  $\delta_{99}$ , equals  $4.92l$ . The same domain lengths are used as for the constant-coefficient problem. In this case, the spectrum consists of a continuous and discrete part. The discrete part is treated separately in Section 5.2.3.

### 5.2.1. Continuous spectrum

The fact that the profiles attain the same asymptotic edge values (super-exponentially) as  $y \rightarrow \infty$  implies that the absolute and essential spectra are identical for the varying-coefficient problem as for the constant-coefficient problem, by the Weyl essential spectrum theorem, see Kapitula and Promislow

[11, theorem 2.2.6] and Kato [18, chapter 4, theorem 5.35]. So, while no analytical solution exists for  $L < \infty$ , the absolute and essential spectrum limits are still equal to their constant-coefficient equivalents.

The  $\hat{\omega}$ -spectra obtained by solving the weighted problem, Eq. (16), are shown in Fig. 7 (a). All  $\hat{\omega}$ -spectra have the shape of a slanted line down to the Nyquist limit. Tracing the spectrum downwards with respect to the branch point, the values of  $\hat{\omega}_r$  move in the negative direction, i.e.  $\hat{\omega}_r < \alpha \bar{U}_e$ . As  $L \rightarrow \infty$ , the computed spectrum converges to the absolute spectrum,  $\hat{\omega}_r \rightarrow \alpha \bar{U}_e$  as expected. This is directly in-line with theorem 5 of Sandstede and Scheel [12]. The slanted shape of the computed spectrum for finite  $L$  is well-known in the literature, e.g. see Antar and Benek [31], Spalart et al. [32] and Maslowe and Spiteri [33], and is related to the fact that  $\bar{U}(y) < \bar{U}_e$  as  $y \rightarrow 0$ . For large but finite domain lengths, the eigenfunctions have a small support inside the boundary layer as opposed to that in the freestream. The value of  $\hat{\omega}_r$  relates to the advection speed that the  $\bar{U}$ -profile exerts on the perturbation. Inside the boundary layer, the flow speed is smaller than  $\bar{U}_e$  and therefore the perturbation is advected at a slightly lower speed, resulting in a smaller  $\hat{\omega}_r$ -value. As  $L \rightarrow \infty$ , the relative extent of the boundary layer diminishes and the real part of all continuum eigenvalues approach  $\alpha \bar{U}_e$  as a consequence.

The  $\hat{\omega}$ -spectra obtained by solving the unweighted problem, Eq. (3), are shown in Fig. 7 (b), again note the different scale for  $\omega_r$  (the scale is same as that in Fig. 3 (b)). The behaviour



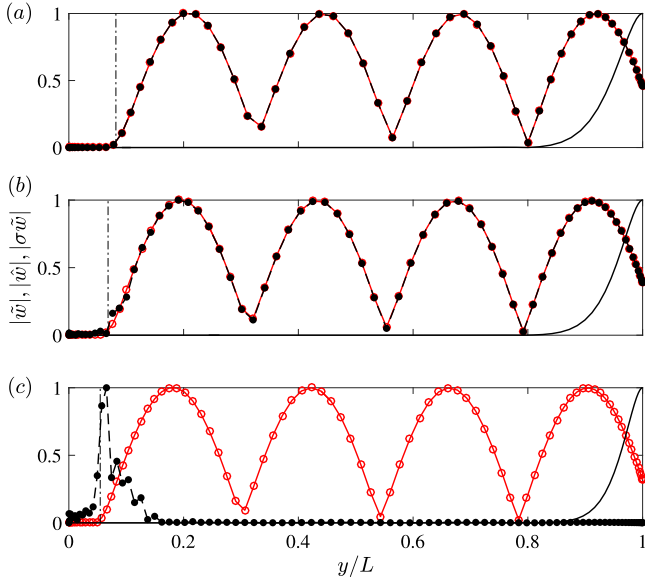


**Fig. 8.** Computed continuum modes  $|\tilde{w}|$  (solid black, unweighted approach) and  $|\hat{w}|$  (solid red, weighted approach) and  $|\sigma\tilde{w}|$  (dashed black, unweighted approach) for comparison, fourth harmonic with  $L/l = N = 60$  (a), 72 (b) and 90 (c).  $\bar{V}_e l/\nu = 1.7208/2$ , all functions are scaled with respect to their maximum value. Boundary-layer thickness  $\delta_{99} = 4.92l$  (dashed-dotted).

of the spectrum is very similar to what is observed for the constant-coefficient case. For small enough  $L$ , the spectrum resides closely to the analytical absolute spectrum. For larger  $L$ , the spectrum again moves away from the absolute spectrum and forms a parabolic shape that approaches the essential spectrum limit. The manner in which the spectrum departs from the absolute spectrum with respect to the constant-coefficient case is investigated. This is done by showing excerpts of the parabolic parts of the corresponding spectra in Fig. 3 (b) as the thin solid lines in Fig. 7 (b). The width of the parabolas corresponding to the constant-coefficient case is larger than that corresponding to the varying-coefficient cases. For an explanation see Section 5.2.2.

With this finding, it is conclusively demonstrated that, also for the problem with varying coefficients, the weighted problem formulation is the appropriate approach to numerically approximate the absolute spectrum, set out as the first objective in the introduction.

### 5.2.2. Continuum eigenfunctions

Whereas the  $\sigma^{-1}\hat{w}$  products and  $\tilde{w}$ -eigenfunctions were studied for the constant-coefficient case, it is more illustrative to consider the  $\hat{w}$ -eigenfunctions and  $\sigma\tilde{w}$  products for the varying-coefficient case. The representative shape of the  $\hat{w}$ -eigenfunctions, obtained with the weighted approach, is illustrated by considering the fourth harmonic continuum mode eigenfunctions in Fig. 8 (now on linear scale). The different panels show the results for different domain lengths; note that the  $y$ -coordinate is scaled with  $L$ . The solid black lines (visible only for  $y/L > 0.8$ ) show the growing character of the unweighted  $\tilde{w}$ -eigenfunctions (and the  $\sigma^{-1}\hat{w}$  products). The weighted eigenfunctions  $\hat{w}$ , shown as the red lines, display no growth from peak to peak for  $y > \delta_{99}$ . The function  $\sigma\tilde{w}$  can be directly compared with  $\hat{w}$ , see Section 4. For sufficiently small  $L$ , both functions are identical, see Fig. 8 (a) and (b). For  $L > L_{th}$ , the truncated magnitude of the  $\tilde{w}$  eigenfunctions for small  $y/l$  causes the match to fail, as represented by Fig. 8 (c). Computational noise dominates the product  $\sigma\tilde{w}$  for small  $y$ , clearly exemplifying the numerical issues encountered when solving the unweighted problem for too large domain lengths.

Inside the boundary layer ( $y < \delta_{99}$ , see the dash-dotted line in Fig. 8), the functions  $|\hat{w}|$  and  $|\sigma\tilde{w}|$  show a significant amplitude reduction (also see Grosch and Salwen [20]; Maslowe and Spiteri [33]). This is clearly related to the strong  $y$ -dependency of the  $\bar{U}$ - and  $\bar{V}$ -profiles in this region. Therefore, one could name this the ‘local effect’ of the varying boundary-layer profiles on the continuum solutions. In fact, note that the use of the Dirichlet boundary condition in the problem with constant-coefficients mimics this behaviour; the amplitudes going to zero. Therefore, the Dirichlet condition could be regarded as a representative model for the local perturbation dynamics in the boundary layer.

In conclusion, the fact that the eigenfunctions approach a zero magnitude inside the boundary layer implies that the eigenfunctions ‘see’ a smaller effective domain length with respect to the constant-coefficient case. Therefore, when deploying the unweighted problem formulation for the varying-coefficient case, the spectrum departs from the analytical absolute spectrum for slightly larger  $L$  than for the constant-coefficient case. Accordingly, the spectra corresponding to the varying-coefficient case lie closer to the absolute spectrum compared to those corresponding to the constant-coefficient case. The latter problem has the largest effective domain length, so it represents the worst case scenario.

### 5.2.3. Discrete solutions

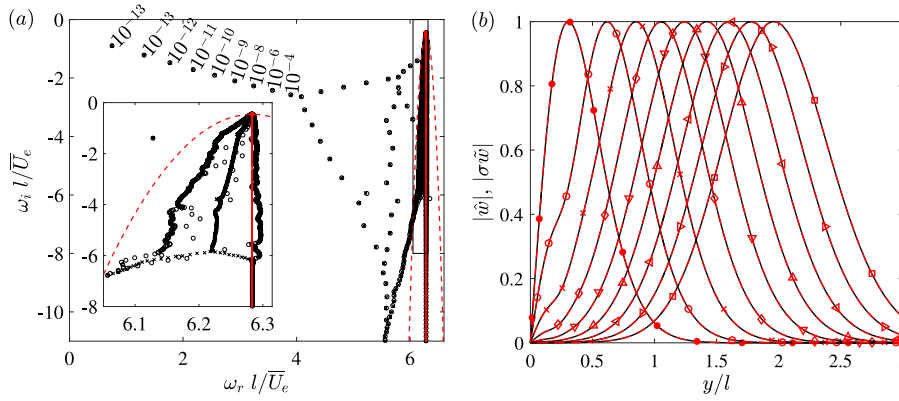
The inhomogeneity of the  $\bar{U}$ - and  $\bar{V}$ -profile introduces  $\delta_{99}$  as a finite length scale. In turn, that causes the spectrum for  $L \rightarrow \infty$  to have a discrete subset with proper eigenmodes that occupy the interior of the boundary layer and decay exponentially for  $y > \delta_{99}$ . The former property implies that  $\omega_r < \alpha\bar{U}_e$ ; the solutions are advected with speeds associated with the interior of the boundary layer. Their decay for increasing  $y$  renders them integrable and thus they are individually interpretable as physical mode shapes. As  $L \rightarrow \infty$ , the properties of these modes converge exponentially, see Sandstede and Scheel [12, lemma 4.3]. Here,  $L/l = 90$  was used to illustrate this part of the spectrum. The discrete solutions require a high resolution close to the boundary at  $y = 0$ . Usually the resolution is increased by using a mapping [25]. As mentioned before, such grid mappings are here avoided because the continuum solutions require both boundaries to be resolved equally well. Therefore, the discrete solutions are underresolved when using  $N = L/l = 90$ ; so  $N = 1000$  was used instead.

Fig. 9 (a) illustrates the complete spectrum for both problem formulations (3) and (16). The eigenvalue errors are shown for the converged eigenvalues with  $\omega_r l/\bar{U}_e < 4$ , comparing the results from the different formulations. For the higher harmonics with larger  $\omega_r$ , the error increases (up to  $10^{-4}\bar{U}_e/l$ ), but remains insignificant with respect to the change ( $10^{-1}\bar{U}_e/l$ ) of the continuum modes, as shown in the inset. The discrete  $\sigma\tilde{w}$  (in black) and  $\hat{w}$  (red) eigenfunctions are shown in Fig. 9 (b). Both formulations produce virtually identical eigenfunctions.

## 6. Eigenfunction representation of wave packets

It was shown in the previous section that the absolute spectrum cannot be resolved on too large domains with the unweighted approach. Nevertheless, this does not necessarily imply that the corresponding bases cannot be used for successful eigenfunction expansions. The goal of this section is to demonstrate that the performance of the weighted approach is superior to that of the unweighted approach in regard to representing arbitrary wave packets through the use of the computed bases in the eigenfunction expansions:

$$w'(0, y, t) = \sum_{j=0}^M \tilde{a}_j \tilde{w}_j(y) e^{-i\tilde{\omega}_j t} = \sigma^{-1}(y) \sum_{j=0}^M \hat{a}_j \hat{w}_j(y) e^{-i\hat{\omega}_j t}, \quad (23)$$



**Fig. 9.** (a) Comparison of discrete parts of (o)  $\tilde{\omega}$ - and (x)  $\hat{\omega}$ -spectrum.  $N = 1000$ ,  $L/l = 90$ ,  $\bar{V}_e l/\nu = 1.7208/2$ . Labels indicate  $|\tilde{\omega} - \hat{\omega}|$ . Inset: zoom on continuous branches. (b) Discrete modes for unweighted (solid black,  $|\sigma \hat{w}|$ ) and weighted (dashed red,  $|\hat{w}|$ ) problem. Profiles from left to right correspond to labelled modes in (a) from left to right.

where  $M$  is the number of modes used. The assessed aspects are the representation of the initial condition, treated in Section 6.1, the growth rate of the wave packet as  $t \rightarrow \infty$ , see Section 6.2, and the number of modes  $M$  required in the expansion, see Section 6.3. Inspiration is taken from Rodríguez et al. [15], who similarly approach a two-dimensional problem.

In what follows, the non-parallel Blasius profiles will be taken for the base flow. The unweighted and weighted problem formulations, resp. Eqs. (3) and (16) and the associated boundary conditions, will be deployed for different domain lengths. The domain lengths  $L/l = 60, 72, 90, 120, 180$  and  $360$  are considered, as done in Section 5. The resolution  $N = L/l$  is chosen once again, so to have an approximately equal resolution per unit of  $y/l$  for different domain lengths.

### 6.1. Eigenfunction expansion of an initial condition

An initial condition is represented by setting  $w'(0, y, 0) = w'_{ic}(y)$ , yielding:

$$\sum_{j=0}^M \tilde{a}_j \tilde{w}_j(y) = \sigma^{-1} \sum_{j=0}^M \hat{a}_j \hat{w}_j(y) = w'_{ic}(y). \quad (24)$$

The expansion coefficients  $\tilde{a}_j$  and  $\hat{a}_j$  are determined through the use of the adjoint eigenfunctions for the respective bases, which can be computed separately with the eigensolver, see Appendix B for more information.

The product of a Gaussian and sine function is chosen as the initial condition:

$$w'_{ic}(y) = e^{-\frac{1}{2} \left( \frac{y-y_w}{\Delta_w} \right)^2} \sin \frac{y-y_w}{\Delta_w} \quad (25)$$

where  $\Delta_w = 3l$  is the width and  $y_w$  is the location of its centre. The main value for  $y_w/l$  is set equal to  $L/l - 12$ , i.e. a specific position that is fixed relative to the truncation boundary. That way, the time duration for the wave packet to propagate out of the domain is equal for all domain lengths.

First, the initial condition is reconstructed with all available eigenmodes in a computed eigenfunction basis; i.e.  $M$  is set equal to  $N$ . Using the bases computed with the weighted approach, the initial condition is successfully resolved for all domain lengths, see Fig. 10 (a). Hence the product  $\sigma^{-1} \hat{w}$ , while growing exponentially in space, can yield a localized, and therefore interpretable, signal by superposing many such functions. The function  $\sigma^{-1}$  is indicated with the dash-dotted line for reference.

When using bases computed with the unweighted approach, the expansion successfully approximates the initial condition for

$L < L_{th} = 73l$ , see Fig. 10 (b). The reconstructed  $w'$ -functions are not rescaled; they are plotted as returned by the eigenfunction expansion. A problem arises for too large domain lengths. For  $L > L_{th}$ , the eigenfunction expansion diverges from the initial condition as  $y \rightarrow L$ . This part of the function is here referred to as a *divergent tail* and is observed in the spatial range where the weighting function  $\sigma^{-1}$  becomes  $O(1)$ . In fact, the function  $\sigma^{-1}$  gives a good representation of the relative amplitude distribution of the divergent tails. This suggests that the tails are caused by the spatial growth of the  $\hat{w}$ -eigenfunctions that, for  $L > L_{th}$ , cannot be properly cancelled out, even if *all* computed eigenmodes are used in the expansion. These tails are obviously problematic for the transient behaviour of the wave packet, but the current interest goes out to the time-asymptotic behaviour of the wave packet, which will be investigated in the next section.

*It is concluded that the weighted approach is the superior method in representing the initial conditions, if only because it does not produce divergent tails.*

### 6.2. Time-asymptotic behaviour

A way of quantifying the evolution of the wave packet is to measure its maximum amplitude inside the domain:

$$A(t) = \max_{y \in [0, L]} |w'(0, y, t)|. \quad (26)$$

The function  $A(t)$  becomes very small for large  $t$ , rendering its numerical measurement impractical. Therefore, the auxiliary amplitude  $A_{aux}$  is obtained with both weighted and unweighted approaches as follows:

$$\begin{aligned} A_{aux}(t) &= A(t) e^{\omega_{aux} t} = \max_y \left| \sigma^{-1} \sum_{j=0}^M \hat{a}_j \hat{w}_j e^{(-i\hat{\omega}_j + \omega_{aux})t} \right| \\ &= \max_y \left| \sum_{j=0}^M \tilde{a}_j \tilde{w}_j e^{(-i\tilde{\omega}_j + \omega_{aux})t} \right|. \end{aligned} \quad (27)$$

The auxiliary growth rate  $\omega_{aux}$  is set equal to the negative of the largest  $\omega_i$ -value in the computed spectrum. The function  $A_{aux}(t)$  does not decay exponentially in time as  $t \rightarrow \infty$ . Note that Eq. (27) serves solely as the definition for  $A_{aux}(t)$  for the different cases; the final equality is valid only if  $\hat{w} = \sigma^{-1} \tilde{w}$ .

The measured instantaneous exponential growth rate of the wave packet is determined as follows:

$$\omega_{m,i}(t) = \frac{d \ln A_{aux}(t)}{dt} - \omega_{aux}, \quad (28)$$

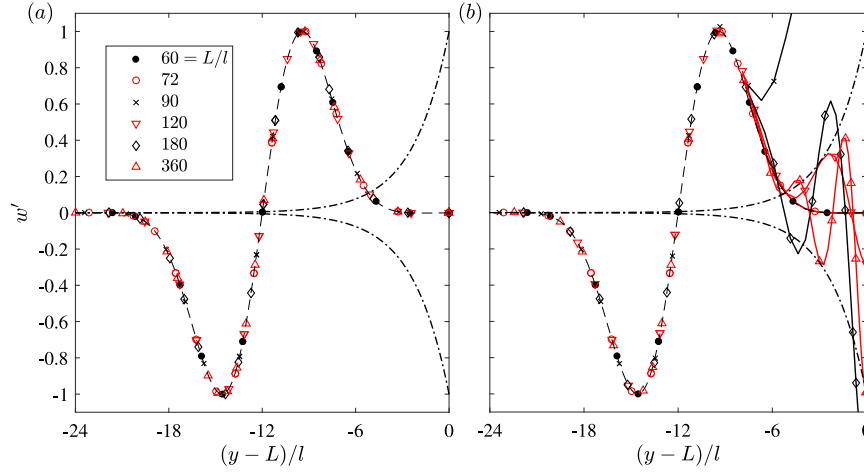


**Fig. 10.** Representation of the initial condition with the eigenfunction bases (symbols) computed with the (a) weighted and (b) unweighted approach for different domain lengths. Exact initial condition (dashed line), weighting function  $\pm\sigma^{-1}$  (dash-dotted line). In (b), the symbols representing the divergent tail are connected with lines for clarity.

where the subscript  $m$  stands for *measured*. For large  $t$ , this growth rate can be compared to the theoretical value provided by Briggs's criterion. This criterion states that the exponential temporal growth rate of wave packets for large  $t$  is dictated by the branch point in the absolute spectrum, i.e.:

$$\omega_{0,i} = -v \left( \alpha^2 + \left( \frac{\bar{V}_e}{2v} \right)^2 \right), \quad (29)$$

for the current model problem, see Eq. (14). The quantity  $\omega_{0,i}$  is here referred to as the absolute growth rate. The long term solution behaviour is given by:

$$\frac{e^{\omega_{0,i}t}}{\sqrt{t}} = e^{\omega_{0,i}t} e^{\ln(t^{-1/2})} = e^{\left(\omega_{0,i} - \frac{\ln(t)}{2t}\right)t}, \quad (30)$$

for  $t \rightarrow \infty$ . The term  $-\ln(t)/2t$  indicates that the measured growth rate  $\omega_{m,i}(t)$  should approach  $\omega_{0,i}$  from below as  $t \rightarrow \infty$ .

The growth rate:

$$\omega_{e,i} = -v\alpha^2, \quad (31)$$

corresponds to the maximum  $\omega_i$ -value attained by the essential spectrum, here referred to as the essential growth rate. It is here defined to demonstrate that this growth rate does *not* have a direct relationship with the time-asymptotic behaviour of wave packets.

As time evolves, the wave packet diffuses and moves one unit of  $l$  in the  $y$ -direction for every time unit  $\Delta t = l/\bar{V}_e$ . The evolution of the measured growth rate  $\omega_{m,i}(t)$ , computed by using the weighted approach, is shown for  $t$  up to  $300\Delta t$  in Fig. 11 (a). There is a clear distinction between the behaviour for  $t < 24\Delta t$  and  $t > 24\Delta t$ . For  $t < 24\Delta t$ , the main structure of the wave packet is still contained in the interior of the domain. When using the weighted approach, this evolution is identical for all domain lengths. For  $t > 24\Delta t$ ,  $\omega_{m,i}(t)$  decreases below  $\omega_{0,i}$  and thereafter approaches  $\omega_{0,i}$  slowly from below, as expected in light of Eq. (30), and thus reflects Briggs's criterion. A well-defined common convergent trend exists as  $L \rightarrow \infty$ .

The evolution of the growth rate recovered with the unweighted approach over the same time range is presented in Fig. 11 (b). The evolution for  $t < 24\Delta t$  differs for different domain lengths  $L > L_{th}$ , as expected due to the large amplitude of the divergent tail of the initial condition. Despite these differences, the curves for all considered domain lengths collapse for the time range  $24 < t/\Delta t < 125$  and they display a slow approach to

$\omega_{0,i}$ , just as observed when using the weighted approach. For  $t > 125\Delta t$ , however, the curves corresponding to the largest domain lengths ( $L/l = 120, 180$  and  $360$ ) diverge from the common trend formed by the smaller domain length cases ( $L/l = 60, 72$  and  $90$ ). It is found that the point at which the curves diverge depends sensitively on the domain length, while being independent of the number of modes  $M$  used in the expansion and the choice of  $\omega_{aux}$ . This is important, for it prohibits the identification of a common convergent trend as  $L \rightarrow \infty$ . The divergence of the curves is expected to be a numerical artefact directly associated to the use of the spatially exponentially growing eigenfunctions of the unweighted problem. The curves are therefore dismissed as representing physical behaviour. *This implies that the time-asymptotic behaviour cannot be identified when the unweighted approach is used with  $L > L_{th}$ .*

Due to the existence of a common convergent trend when the weighted approach is used as  $L \rightarrow \infty$ , it is meaningful to assess the behaviour of the wave packets for much larger times in that case. The evolution of the growth rate for  $t$  up to  $10^4\Delta t$  is shown in Fig. 12. It is observed that  $\omega_{m,i}$  deviates from the common trend for a given domain length for large enough times; specifically, it saturates at the maximum  $\omega_i$ -value in the computed spectrum. For larger domain lengths, the deviation becomes smaller. So, this demonstrates that *the  $\omega_{m,i}$  curves computed with the weighted approach consistently converge to the absolute growth rate  $\omega_{0,i}$  as  $L \rightarrow \infty$ .*

### 6.3. Required number of modes

Up to now, all  $N$  available modes have been used to represent the wave packet dynamics. Ignoring the previous negative conclusions for the unweighted approach, the question remains whether a different number of modes is required when using the basis of  $\tilde{w}$ - and  $\hat{w}$ -solutions.

The focus is again put on the time-asymptotic behaviour. It is deemed fairest to compare the number of modes required to represent the wave packet behaviour in the time range  $24 < t/\Delta t < 125$ , because the behaviour is the same for all domain lengths and the different approaches. The growth rate at the time  $t = 120\Delta t$  is chosen specifically, for the common trend of  $\omega_{m,i}(t)$  for the weighted and unweighted approaches is to tend toward  $\omega_{0,i}$  at that time.

One would expect that the modes with the largest  $\omega_i$  will dictate the time-asymptotic behaviour. Therefore,  $M$  modes with the largest  $\omega_i$ -values are chosen in the expansions (24) with

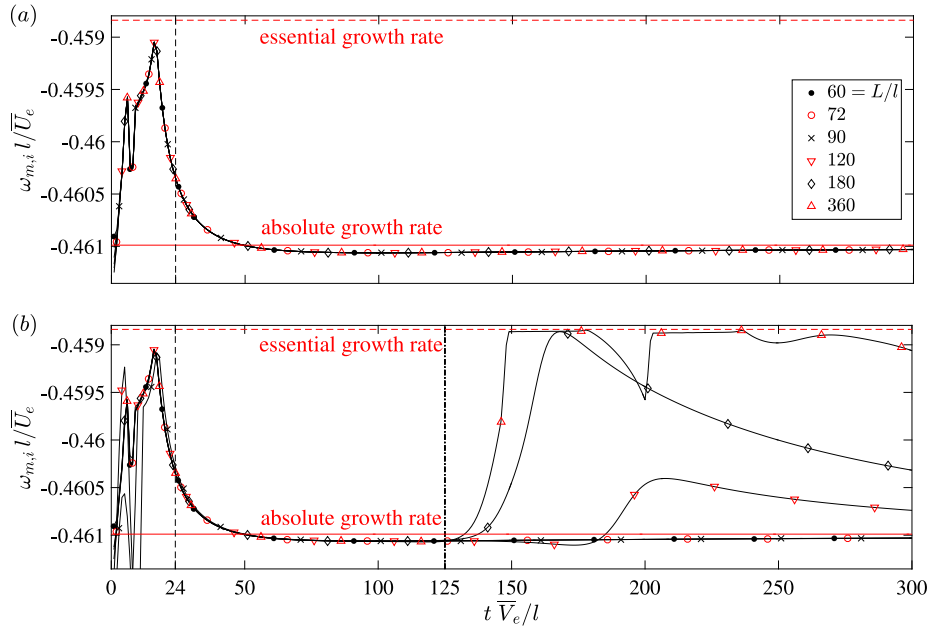


**Fig. 11.** Intermediate time evolution of the measured exponential growth rate of the wave packet reconstructed with bases computed with the (a) weighted and (b) unweighted approach for different domain lengths.  $\omega_{0,i}$  (red solid line),  $\omega_{e,i}$  (red dashed line),  $t = 24\Delta t$  (black dashed line) and  $t = 125\Delta t$  (black dash-dotted line).

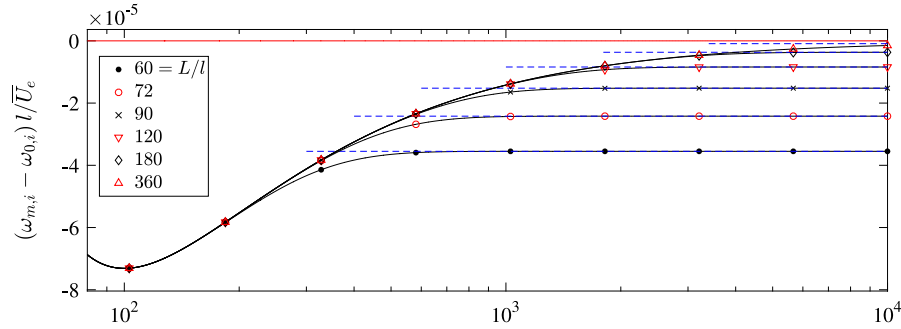


**Fig. 12.** Long time evolution of the measured exponential growth rate of the wave packet reconstructed with bases computed with the weighted approach for different domain lengths. Maximum  $\omega_i$ -value attained by the computed spectrum (blue dashed lines),  $\omega_{0,i}$  (red solid line) and  $\omega_{e,i}$  (red dashed line).

$M < N$ . The number of modes used is indicated by replacing the argument  $t$  of  $\omega_{m,i}$  by  $M$ :  $\omega_{m,i}(M)$ . The value  $\omega_{m,i}(N)$ , i.e. with  $M = N$ , is taken as the reference per domain length and method.

The resulting convergence graphs are shown in Fig. 13. Fig. 13 (a) represents the weighted problem case. For large  $M$ , the error displays a quadratic trend on linear-logarithmic scale (see the black dashed line). As the domain length increases, it is observed that the curves tend toward larger  $M$ -values, indicating that more modes are required to represent the dynamics. This is reasonable from the perspective that the extent of the wave packet,  $\Delta_w$ , is held fixed while the domain length is increased.

The convergence curves obtained when using the unweighted approach are presented in Fig. 13 (b). The black dashed and dash-dotted lines are the same in the subfigures 13 (a) and (b) and clarify the relative differences. For small enough domain lengths, i.e.  $L < L_{th}$ , the errors are virtually identical to those obtained with the weighted method. For too large domain lengths, however, the situation is very different. Most important to note is that, for  $M/N < 10\%$  and large  $L$ , the convergence curve displays a distinct plateau. This indicates that, contrary to the expectation, the first 10% of the modes with the largest growth rates do *not* contribute to the wave packet behaviour of interest. This implies that many more modes are required to represent the wave packet up to the same accuracy when deploying the unweighted as opposed to the weighted approach.

*In conclusion with respect to the representation of wave packets, the weighted approach enjoys a superior performance over the unweighted approach in regard to all aspects (viz. producing the initial condition and the time-asymptotic behaviour and the required number of modes to do so).*

## 7. Conclusion

The study of the linear stability of flows (e.g. solutions of the Navier–Stokes equations) requires the solution of differential-eigenvalue problems posed on (semi-)infinite domains. In these eigenvalue problems, the spectrum of eigenvalues represents the temporal character and the corresponding eigenfunctions the spatial character of the solution. Exact solutions are seldomly available and solutions are therefore usually approximated numerically. To obtain the eigenvalues and -functions numerically, one has to truncate the domain length  $L < \infty$  and introduce artificial truncation boundary conditions. Usually, separated (e.g. Dirichlet, Neumann or Robin type) boundary conditions are considered, see Ehrenstein and Gallaire [13]; Alizard and Robinet [14]; Åkervik et al. [34]; Rodríguez et al. [15]. Computing the limit of the spectrum as  $L \rightarrow \infty$  is troublesome, however, if the operator supports advective processes throughout the domain. These processes cause the eigenfunctions to grow exponentially



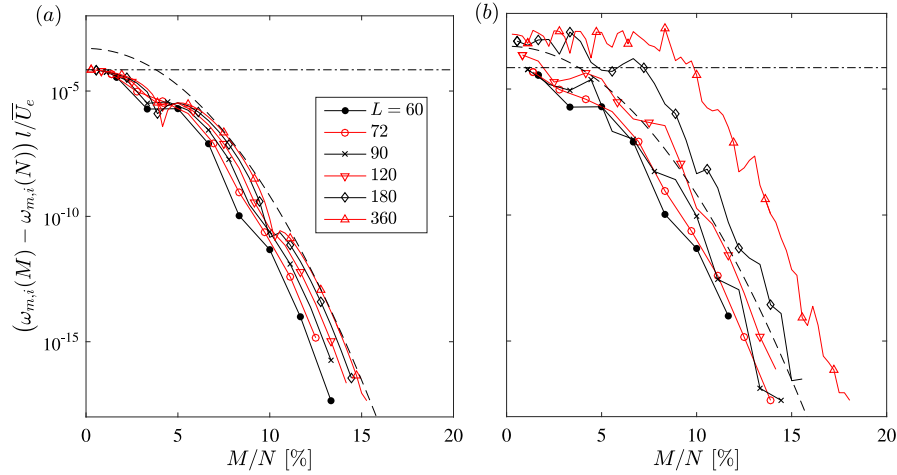


**Fig. 13.** Convergence of the wave packet's growth rate at  $t = 120\Delta t$  with respect to the number of modes  $M$  using (a) the weighted and (b) unweighted approach. The reference growth rate is computed per domain length and used method at  $t = 120\Delta t$  using  $M = N$ .

in the advection direction. Therefore, if their maximum magnitude is scaled to unity, the eigenfunctions attain arbitrarily small absolute magnitudes elsewhere in the domain and this yields numerical underflow errors. This causes the sensitivity of the computed spectrum on the choice for the truncation boundary conditions and domain length. Moreover, the computed spectrum diverges from the mathematically correct limit of the spectrum as the domain length is increased.

The main result of this paper is that:

*The correct spectrum limit can be approximated numerically by using the proposed weighted approach as  $L \rightarrow \infty$ . This is crucial for the identification of the absolute stability of a considered base flow.*

The weighted approach removes the advection-induced spatial exponential growth from the eigenfunctions and therefore eliminates the cause for the numerical underflow errors. Accordingly, the limit of the spectrum as  $L \rightarrow \infty$  can be accurately approximated numerically. Using separated boundary conditions, the computed spectra converge to the absolute spectrum for all considered  $L \rightarrow \infty$ , which is in accordance with theorem 5 of Sandstede and Scheel [12]. This demonstrates that *the approximation of the continuous spectrum does converge as  $L \rightarrow \infty$* . This directly contradicts the statement of Theofilis [3] quoted in the introduction.

The absolute spectrum contains branch points and is therefore interpretable in light of Briggs's criterion for absolute instability, i.e. the base flow supports an absolute instability only if the absolute spectrum is unstable, see Briggs [7]; Huerre and Monkewitz [8]; Brevdo [9]; Schmid and Henningson [5]. When the spectrum is obtained using the unweighted approach, it tends to the essential spectrum as  $L \rightarrow \infty$ . Since this spectrum limit does not contain branch points, the absolute stability of the base flow cannot be deduced from the numerical results obtained with the unweighted approach.

Concerning the representation of spatially localized wave packets, the performance of the weighted method is also superior to that of the unweighted approach. Only when using the weighted approach, the initial condition is accurately represented for arbitrary domain lengths and the long-term time evolution is consistent with Briggs's criterion. Furthermore, accurate results can be obtained using a limited number of eigenmodes.

## Appendix A. Interpretation spatial growth & symmetrization

The spatial exponential growth of the  $\tilde{w}$ -solutions suggests that the  $\tilde{w}$ -problem is somehow ill-posed. The aim of this appendix is to point out the core of this issue and demonstrate how symmetrization resolves it.

An eigensolution is per definition composed out of two parts: an 'eigenfunction part', that represents the solution's shape in space, and an 'eigenvalue part', that scales the amplitude of the eigenfunction in time. So, eigensolutions preserve their shape in time.

To identify whether a system supports convectively or absolutely unstable solutions, the solution must have a finite support in space, as mentioned in the introduction. Per definition, advective processes translate any signal in the advection direction as time evolves. *Representing a translation of the finite-support solutions of interest with eigensolutions is problematic, because a spatial displacement cannot be represented by scaling the amplitude of an eigenfunction with a finite support.*

Advective processes can still be represented by eigensolutions by allowing the eigenfunctions to grow exponentially in the direction of the advection. This follows directly by considering the exponential function as an example. Scaling it with any positive constant  $c > 0$  is equivalent to translating it in the spatial direction:

$$c e^y = e^{y + \ln c}, \quad (\text{A.1})$$

where  $c < 1$  and  $c > 1$  correspond to a shift in the positive and negative  $y$ -direction, respectively. *When advective processes remain active infinitely far in space, the eigenfunctions must grow indefinitely and therefore are required to have an infinite support.*

By considering a specific perturbation with a finite support that is representative of a solution of the advection-diffusion equation, the link between the advection-induced translation and the exponential growth of the eigensolutions can be clearly demonstrated. Furthermore, it directly shows where the factor  $\nu(\bar{V}_e/2\nu)^2$  in  $\omega_0$  and the weighting function  $\sigma^{-1}(y)$  come from in the case of constant coefficients, see Eqs. (29) and (15), respectively.

As a specific perturbation, we can consider a wave packet with a Gaussian shape that translates and broadens in  $y$  and whose amplitude decays in time:

$$w'(0, y, t) = \underbrace{e^{-(y - \bar{V}_e t)^2 / 4\nu t}}_{\text{translates and broadens in } y} \times \underbrace{e^{-\nu \alpha^2 t / \sqrt{t}}}_{\text{constant in } y} \frac{d(t; \alpha^2)}{d(t; \alpha^2)},$$

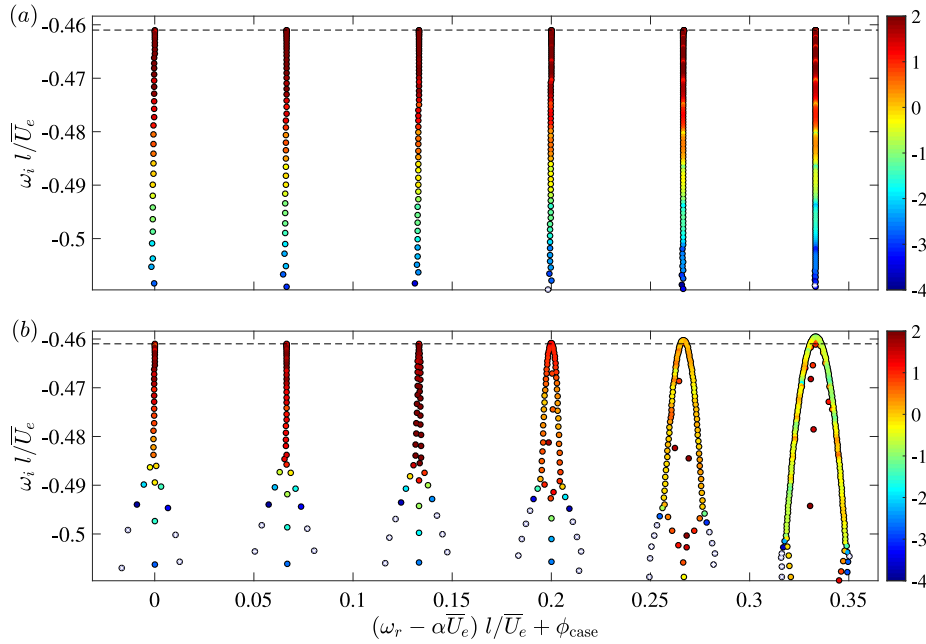


**Fig. B.14.** Spectra colour-coded with the size of the expansion coefficients using the bases computed with the (a) weighted and (b) unweighted approaches for different lengths:  $L/l = 60$  ( $\phi_{\text{case}} = 0$ ), 72 (1/15), 90 (2/15), 120 (1/5), 180 (4/15) and 360 (1/3). Modes that have coefficients with a magnitude smaller than  $10^{-4}$  are indicated with a white cross. Absolute growth rate (dashed line).

Rewriting this expression, results in:

$$= \underbrace{e^{\bar{V}_e y / 2\nu}}_{\sigma^{-1}(y)} \times \underbrace{e^{-y^2 / 4\nu t}}_{g(y, t)} \times \underbrace{e^{-\nu(\alpha^2 + (\bar{V}_e / 2\nu)^2)t} / \sqrt{t}}_{d(t; \alpha^2 + (\bar{V}_e / 2\nu)^2)},$$

spatial growth factor      only broadens in  $y$       constant in  $y$

where the first factor,  $\sigma^{-1}$ , represents the spatial exponential growth in  $y$ , the second,  $g(y, t)$ , the broadening in  $y$  and the third,  $d$ , the amplitude decaying in time. It is very insightful to notice that  $g(y, t)$  is ‘stationary,’ even though it broadens, *the advection-induced translation is removed*. The spatially exponentially growing function  $\sigma^{-1}(y)$  reinstates the advection-induced translation. I.e. without this factor, the first expression is recovered without the translation effect due to  $\bar{V}_e$ .

When using eigenfunctions to build this particular  $w'$ , the unweighted or weighted approaches can be used. When considering the weighted approach, on the one hand, one constructs the non-translating function  $g(y, t)d(t; \alpha^2 + (\bar{V}_e / 2\nu)^2)$  with eigenfunctions that stay bounded in space, which are relatively easy to resolve numerically. On the other hand, using the unweighted approach, one has to represent the translation of the wave packet, which requires an advection-induced spatial growth in the unweighted eigenfunctions, which is very difficult to represent numerically.

The above very clearly illustrates the essential working principle of symmetrization. By factoring  $\sigma^{-1}$  from the eigenfunctions, the troublesome advection-induced translation is removed and the remaining solution dynamics can be captured effectively with the eigensolutions.

In removing the advection-induced translation, *symmetrization is very much like transforming the problem to a moving reference frame*. It should be noted, however, that the obtained eigensolutions still correspond to the stationary reference frame. Therefore, it could be argued that symmetrization makes use of the moving reference frame ‘under the hood’ only. It is hard to generalize the symmetrization method to higher (differential) order problems. Therefore, it is recommended to transform more difficult problems to a reference frame that moves with the local advection velocity, i.e. following the base flow. Extra difficulties are expected

in that case, but such an approach is expected to circumvent the dramatic numerical issues related to the spatial exponential growth of the eigenfunctions by using the same working principle responsible for the effectiveness of symmetrization.

A possibly unsuspected consequence of the moving-reference-frame interpretation is the conceptual resolution of the issue of the unknown truncation boundary condition. The truncation boundary can be made to move with the local advection speed exactly, because the base flow is known. If this is ensured, the solution is expected to be a standing wave at the boundary. This can be represented exactly by a Neumann (or Robin) type truncation boundary condition.

## Appendix B. Bi-orthogonality relationships

If the relationship  $\tilde{w} = \sigma^{-1}\hat{w}$  holds, then  $\tilde{w}_j$  and  $\hat{w}_j$  have the same expansion coefficient:  $a_j = \tilde{a}_j = \hat{a}_j$ . An approach to determining the expansion coefficients, is using the orthonormality of the  $\hat{w}$ -solutions, i.e. the  $\hat{w}$ -solutions can be scaled such that  $\langle \hat{w}_j, \hat{w}_k \rangle = \delta_{jk}$ , where  $\langle \cdot, \cdot \rangle$  denotes the  $L^2$  inner product and  $\delta_{jk}$  the Kronecker delta. By substituting expansion (24) into the inner product of  $w'_{IC}$  with  $\hat{w}_j\sigma$ , one finds:

$$\begin{aligned} \langle \hat{w}_j\sigma, w'_{IC} \rangle &= \left\langle \hat{w}_j, \sigma \sigma^{-1} \sum_{k=0}^M a_k \hat{w}_k \right\rangle \\ &= \sum_{k=0}^M \langle \hat{w}_j, a_k \hat{w}_k \rangle = \sum_{k=0}^M a_k \delta_{jk} = a_j. \end{aligned} \quad (\text{B.1})$$

Note that  $\sigma$  could be freely exchanged, because it is real-valued. By using that  $\hat{w} = \sigma \tilde{w}$ , an expression involving the  $\tilde{w}$ -solutions follows directly from Eq. (B.1):

$$a_j = \langle \sigma^2 \tilde{w}_j, w'_{IC} \rangle. \quad (\text{B.2})$$

However, the relationship  $\tilde{w} = \sigma^{-1}\hat{w}$  breaks down when the  $\tilde{w}$ -solutions are computed on a too large domain. Therefore Eq. (B.2) cannot be used in that case and  $\tilde{a}_j$  is no longer equal to  $\hat{a}_j$ ; a different method to determine the expansion coefficients

must be resorted to. Whereas the above equations rely upon the orthonormality of the  $\hat{w}$ -solutions, every set of eigenfunctions is bi-orthogonal to the corresponding set of adjoint eigenfunctions. By scaling the functions properly, the bi-orthogonality condition can be expressed as  $\langle \tilde{w}_j^{\text{adj}}, \tilde{w}_k \rangle = \delta_{jk}$  for the  $\tilde{w}$ -solutions, here  $\tilde{w}_j^{\text{adj}}$  is the adjoint function corresponding to  $\tilde{w}_j$ . Note that  $\hat{w}_j^{\text{adj}} = \hat{w}_j$ , because the problem for  $\hat{w}$  is self-adjoint, as mentioned in Section 4. Expressions for the expansion coefficients involving the adjoint eigenfunctions can be derived in a similar way as Eq. (B.1), the final expressions read:

$$\begin{aligned} a_j &= \langle \hat{w}_j^{\text{adj}}, \sigma w'_{\text{IC}} \rangle = \langle \hat{w}_j, \sigma w'_{\text{IC}} \rangle \\ &= \langle \tilde{w}_j^{\text{adj}}, w'_{\text{IC}} \rangle = \langle \sigma^2 \tilde{w}_j, w'_{\text{IC}} \rangle \end{aligned} \quad (\text{B.3})$$

where the final equation, which equates  $\tilde{w}_j^{\text{adj}} = \sigma^2 \tilde{w}_j$ , is recovered numerically for small enough domain lengths only. It is interesting to note that, in absence of numerical errors, the spatial growth rates of  $\tilde{w}$  and the corresponding adjoint eigenfunction are equal, but they have the opposite sign, see Chomaz [6].

To fairly compare the performance of the weighted and unweighted approaches in Section 6.1, the expansion coefficients are computed by using the adjoint eigenfunctions for both approaches.

To illustrate the behaviour of the expansion coefficients for different domain lengths, the spectra for all cases are illustrated in Fig. B.14, shifted in the real direction with  $\phi_{\text{case}}$  for clarity purposes. The size of the expansion coefficients is indicated with colour. For small enough domain lengths and large enough  $\omega_i$ , the coefficients match for both approaches, while for  $L > L_{\text{th}}$  the coefficients for the unweighted case deviate from those obtained with the weighted basis.

## References

- [1] L. Mack, Special course on stability and transition of laminar flow, in: AGARD, Special Course of Stability and Transition of Laminar Flows, North Atlantic Treaty Organization, 1984.
- [2] H.L. Reed, W.S. Saric, D. Arnal, Linear stability theory applied to boundary layers, *Annu. Rev. Fluid Mech.* 28 (1) (1996) 389–428.
- [3] V. Theofilis, Advances in global linear instability analysis of nonparallel and three-dimensional flows, *Prog. Aerosp. Sci.* 39 (4) (2003) 249–315.
- [4] P. Huerre, P.A. Monkewitz, Local and global instabilities in spatially developing flows, *Annu. Rev. Fluid Mech.* 22 (1) (1990) 473–537.
- [5] P.J. Schmid, D.S. Henningson, *Stability and Transition in Shear Flows*, Springer, 2001.
- [6] J.-M. Chomaz, Global instabilities in spatially developing flows: non-normality and nonlinearity, *Annu. Rev. Fluid Mech.* 37 (2005) 357–392.
- [7] R.J. Briggs, Electron-stream interaction with plasmas, in: M.I.T. Press Research Monographs, M.I.T. Press, 1964.
- [8] P. Huerre, P.A. Monkewitz, Absolute and convective instabilities in open shear layers, *J. Fluid Mech.* 159 (1985) 151–168.
- [9] L. Brevdo, Three-dimensional absolute and convective instabilities, and spatially amplifying waves in parallel shear flows, *Z. Angew. Math. Phys.* 42 (6) (1991) 911–942.
- [10] K.J. Groot, BiGlobal Stability of shear flows - spanwise & streamwise analyses (Ph.D. thesis), Delft University of Technology, 2018.
- [11] T. Kapitula, K. Promislow, *Spectral and Dynamical Stability of Nonlinear Waves*, Springer, 2013.
- [12] B. Sandstede, A. Scheel, Absolute and convective instabilities of waves on unbounded and large bounded domains, *Physica D* 145 (3–4) (2000) 233–277.
- [13] U. Ehrenstein, F. Gallaire, On two-dimensional temporal modes in spatially evolving open flows: the flat-plate boundary layer, *J. Fluid Mech.* 536 (2005) 209–218.
- [14] F. Alizard, J.C. Robinet, Spatially convective global modes in a boundary layer, *Phys. Fluids* 19 (11) (2007).
- [15] D.A. Rodríguez, A. Tumin, V. Theofilis, Towards the foundation of a global modes concept, in: 6th AIAA Theoretical Fluid Mechanics Confer, 2011, pp. 1–18.
- [16] M. Brynjell-Rahkola, N. Shahriari, P. Schlatter, A. Hanifi, D.S. Henningson, Stability and sensitivity of a cross-flow-dominated Falkner–Skan–Cooke boundary layer with discrete surface roughness, *J. Fluid Mech.* 826 (2017) 830–850.
- [17] F. White, *Viscous Fluid Flow*, McGraw-Hill Professional Publishing, 1991.
- [18] T. Kato, *Perturbation Theory for Linear Operators*, vol. 132, Springer, 2013.
- [19] M. Bouthier, Sur la stabilité des écoulements non parallèles et le spectre continu, *C. R. Math. Acad. Sci. Paris* 296 (1983).
- [20] C.E. Grosch, H. Salwen, The continuous spectrum of the Orr–Sommerfeld equation. Part 1. The spectrum and the eigenfunctions, *J. Fluid Mech.* 87 (1978) 33–54.
- [21] R. Haberman, *Applied Partial Differential Equations: With Fourier Series and Boundary Value Problems*, Pearson Education, Limited, 2012.
- [22] S.C. Reddy, L.N. Trefethen, Pseudospectra of the convection-diffusion operator, *SIAM J. Appl. Math.* 54 (6) (1994) 1634–1649.
- [23] C. Canuto, M. Hussaini, A. Quarteroni, T. Zang, *Spectral Methods: Fundamentals in Single Domains*, Springer, 2006.
- [24] J.A.C. Weideman, S.C. Reddy, A MATLAB differentiation matrix suite, *ACM Trans. Math. Software* 26 (4) (2000) 465–519.
- [25] M.R. Malik, Numerical methods for hypersonic boundary layer stability, *J. Comput. Phys.* 86 (2) (1990) 376–413.
- [26] G.H. Golub, C.F. Van Loan, *Matrix Computations*, Johns Hopkins University Press, 1996.
- [27] D.A. Rodríguez, Global instability of laminar separation bubbles (Ph.D. thesis), Universidad Politécnica de Madrid, 2010.
- [28] L.N. Trefethen, M. Embree, *Spectra and Pseudospectra: The Behavior of Nonnormal Matrices and Operators*, Princeton University Press, 2005.
- [29] L. Lesshafft, Artificial eigenmodes in truncated flow domains, *Theor. Comput. Fluid Dyn.* 32 (3) (2018) 245–262.
- [30] E. Anderson, Z. Bai, C. Bischof, L.S. Blackford, J. Demmel, J.J. Dongarra, J. Du Croz, S. Hammarling, A. Greenbaum, A. McKenney, D. Sorensen, *LAPACK Users' Guide*, third ed., Society for Industrial and Applied Mathematics, Philadelphia, 1999.
- [31] B.N. Antar, J.A. Benek, Temporal eigenvalue spectrum of the Orr–Sommerfeld equation for the Blasius boundary layer, *Phys. Fluids* 21 (2) (1978) 183–189.
- [32] P.R. Spalart, R.D. Moser, M.M. Rogers, Spectral methods for the Navier–Stokes equations with one infinite and two periodic directions, *J. Comput. Phys.* 96 (2) (1991) 297–324.
- [33] S.A. Maslowe, R.J. Spiteri, The continuous spectrum for a boundary layer in a streamwise pressure gradient, *Phys. Fluids* 13 (5) (2001) 1294–1299.
- [34] E. Åkervik, U. Ehrenstein, F. Gallaire, D.S. Henningson, Global two-dimensional stability measures of the flat plate boundary-layer flow, *Eur. J. Mech. B Fluids* 27 (5) (2008) 501–513.